A Review of the Single-Step Flame Synthesis of Defective and Heterostructured TiO$_2$ Nanoparticles for Photocatalytic Applications

Sovann Khan [1,*], Jin-Sung Park [2] and Tatsumi Ishihara [1,3,4]

[1] Advanced Energy Conversion Systems Thrust, International Institute for Carbon-Neutral Energy Research, (WPI-I2CNER), Kyushu University, 744 Motooka, Nishi-ku, Fukuoka 819-0395, Japan

[2] Department of Nuclear Science and Engineering, Massachusetts Institute of Technology, Cambridge, MA 02139, USA

[3] Department of Automotive Science Graduate, School of Integrated Frontier Sciences, Kyushu University, 744 Motooka, Nishi-ku, Fukuoka 819-0395, Japan

[4] Department of Applied Chemistry, Faculty of Engineering, Kyushu University, 744 Motooka, Nishi-ku, Fukuoka 819-0395, Japan

* Correspondence: khan.sovann.455@m.kyushu-u.ac.jp

Abstract: Titanium dioxide (TiO$_2$) is an excellent UV-photocatalytic material that is widely used in various applications, including clean energy production, environmental remediation, and chemical production. However, the use of TiO$_2$ is limited in the field of visible light photocatalysis due to its large bandgap and fast recombination rate between electron and hole pairs, which generally results in a low photocatalytic reaction. Defect/bandgap engineering by doping and the introduction of heterojunctions has been successfully employed to improve the photocatalytic activities of TiO$_2$ over a wide wavelength. To apply the unconventional structured TiO$_2$ with high photocatalytic performance to industries, the development of efficient methods for large-scale production is of high importance. Flame synthesis is a very promising method for the rapid production of nanoparticles. In this article, we summarize the latest reports on the synthesis of defective and heterostructured TiO$_2$ using the single-step method of flame synthesis. Fundamental understandings of reactor configurations, synthesis conditions, precursor preparation and their physicochemical properties are intensively discussed.

Keywords: flame synthesis; TiO$_2$; doping and heterojunction; photocatalysis

1. Introduction

Titanium dioxide (TiO$_2$) is a semiconductor material that is commercially used in construction (e.g., paints and coating materials), health care, cosmetics, environment and energy [1–3]. Concerning the global issues of environmental pollution, the use of TiO$_2$ as a photocatalyst has become more attractive due to its strong redox properties, nontoxicity and earth abundance. The demand of TiO$_2$ keeps increasing year by year. It was reported that the global market of TiO$_2$ was approximately USD 17.19 billion in 2020, and it is expected to grow over 6% CAGR from 2021 to 2028 [4]. Therefore, it is foreseen that the production of high-quality TiO$_2$ would be more competitive to take a share of this market. There are many world-class manufacturers (e.g., Chemours, Cristal, Evonik-Degussa, Huntsman, Ishihara Sangyo, Kronos, Lomon-Billions and Tronox [5]) commercially producing this material, mainly for paints and coatings, plastic, pulp and paper, and cosmetics. However, it is still very challenging to produce highly active TiO$_2$ as a photocatalyst, typically for visible-light photocatalysis.

Anatase and rutile are major crystalized phases of TiO$_2$, and they are highly stable and commonly known as active photocatalysts. In addition, the metastable phases of TiO$_2$, such as brookite and bronze (B), were also reported as active photocatalysts [6,7]. TiO$_2$ is

a large-bandgap semiconductor (3.2 eV, anatase [8]), which activates under UV light only. When light energy that is equal to or higher than the bandgap energy of TiO$_2$ is radiated, electrons (e$^-$) are excited to the conduction band (CB), leaving holes (h$^+$) at the valence band (VB) (see Figure 1a). Electrons and holes are active species in photocatalysis for reduction and oxidation reactions, respectively. These photogenerated electrons and holes are active species for various chemical reactions. With a strong redox ability, TiO$_2$ is utilized for various applications, such as organic synthesis for value-added products/chemicals [9–11], environmental clean-up/pollutant removals (e.g., dye decomposition and microorganism de-activation [12–14]) and energy (e.g., solar cells and H$_2$ productions [15]) (see Figure 1a).
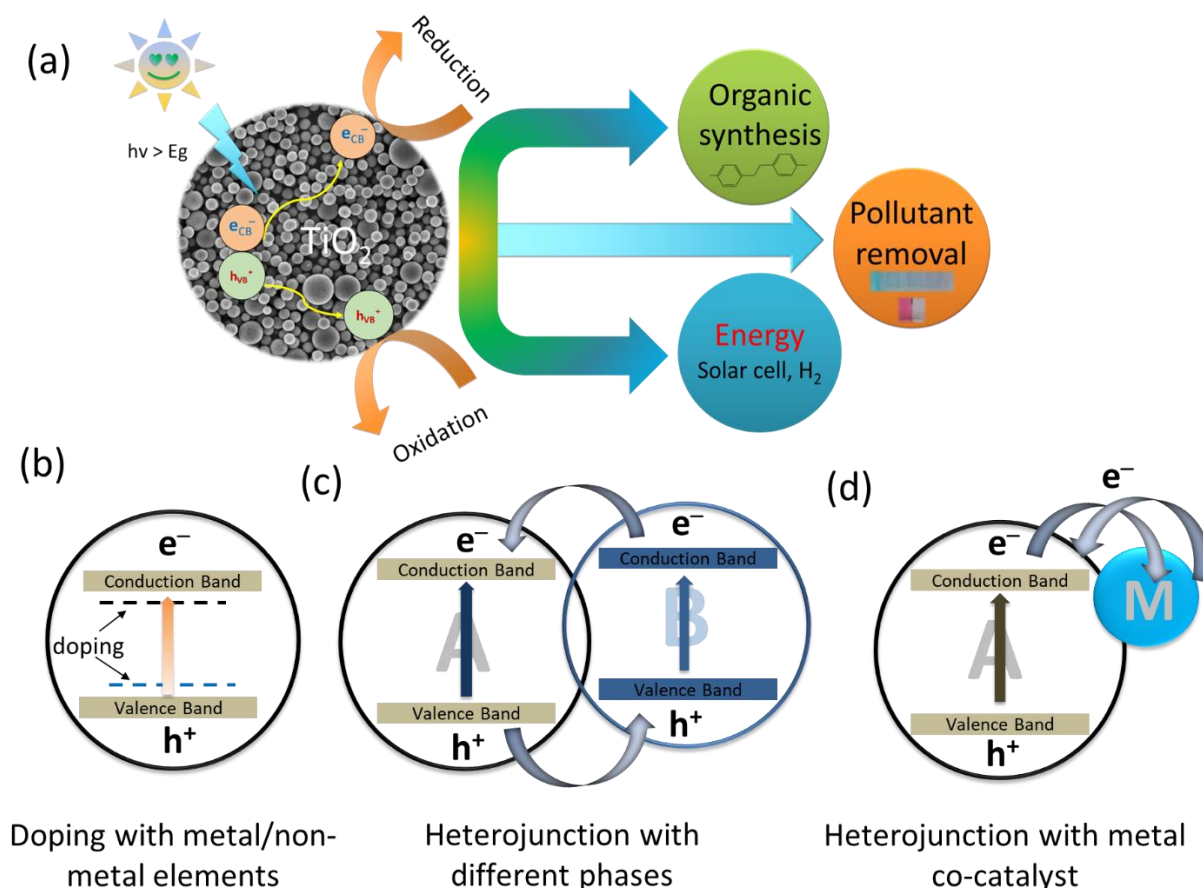
Figure 1. (**a**) Photocatalytic reaction by TiO$_2$ and their applications; (**b**) doping effects; (**c**) heterojunction with other semiconductors or phases; (**d**) heterojunction with metal cocatalyst.

Unfortunately, the catalytic activities of pristine TiO$_2$ are still under limitations: (a) inactivity in visible light, which is abundant in solar spectrum and (b) rapid electron–hole pair recombination, which shortens the life time of the charge carriers for chemical reactions. To overcome these issues, various bandgap engineering methods have been developed to improve the catalytic activities of TiO$_2$. (1) Defect engineering: It has been widely reported that native defects (e.g., oxygen vacancies, Ti^{3+} and interstitial Ti^{4+} [16–19]) and doping defects largely affect the catalytic activities of TiO$_2$ [20,21]. The defects created by metal and non-metal doping are used to create energy levels inside the bandgap for narrowing the bandgap energy of TiO$_2$ to absorb the visible range and facilitate the photo-induced charge separation (Figure 1b). (2) Heterojunction: The recombination rate between electron and hole pairs can be suppressed by the construction of heterojunctions between different crystal phases or materials, resulting in the elongation of the life time of active species for chemical reactions [22–24]. A heterojunction can be created by combining two or more crystal phases, such as anatase–rutile [25–27], anatase–bronze [28], anatase–rutile–bronze [29] and anatase–brookite [30,31]. Alternatively, there are a num-

ber of semiconductors reported to have suitable band alignment with TiO_2 for making heterojunctions, including TiO_2-SiO_2 [32–34], $SrTiO_3$-TiO_2 [35,36], TiO_2-ZnO [37–39] and TiO_2-ZrO_2 [13,40]. With suitable band alignment, photo-induced electrons or holes transfer from one phase to others or from one semiconductor to others, which effectively separates these pairs and provides a higher chance for reactions (Figure 1c). Furthermore, constructing heterojunctions with metal cocatalysts such as noble metals (Pt, Rh, Ru and Pd [41–43]) and non-noble metals (Ni, Co and Cu [44,45]) was also successfully utilized for enhanced catalytic activities. It is well understood that loading metal nanoparticles improves the photo/catalytic reaction of semiconductors based on three main factors: (1) reduction of the activation energy (overpotential) on the surface of a semiconductor [46]; (2) improvement of the electron–hole separation [47] and (3) visible-light harvesting via plasmonic effects [48–50] (Figure 1d).

Therefore, defective and heterostructured TiO_2 nanoparticles exhibit higher catalytic activity over pristine ones. Many studies have been conducted to develop efficient methods to synthesize these unconventional structures of TiO_2. Wet chemical methods are generally used to synthesize various kinds of nanomaterials. However, wet chemical methods might not be preferred for large-scale productions for industrial purposes due to the complexity of scaled-up technologies, the large amount of aqueous waste and high-energy consumption by post-annealing [51,52]. Gas-phase synthesis has been highlighted as a potential method for the large-scale production of nanoparticles, from single to complex components [51,53]. Our research group has been developing various kinds of gas-phase reactors, such as chemical vapor synthesis (CVS) [25], flame synthesis (FS) [51,52,54], plasma-assisted spray/vapor synthesis (PSVS) [55] and spray pyrolysis synthesis (SPS) [56–60], for producing many kinds of nanomaterials used as catalysts, luminescent materials and batteries. Among these reactors, flame synthesis has shown to have a greater potential in the rapid production of nanomaterials, including TiO_2 nanoparticles. Summaries and intensive reviews have been reported in a few earlier publications [61–64], focusing on a broad range of nanoparticles. In this review, we summarize flame synthesis focusing only on TiO_2 production, typically used as a potential synthesis method for multijunction and defect-containing TiO_2 nanoparticles using a single-step process.
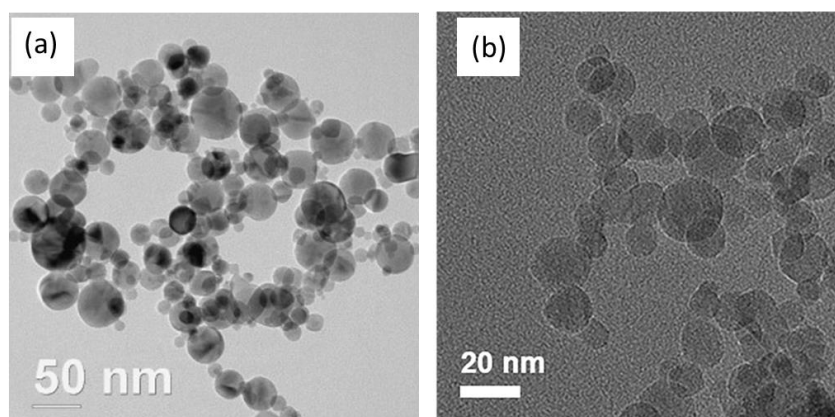
2. Flame Synthesis (FS)

FS is among gas-phase syntheses, and it is considered as a very promising route for the rapid production of nanoparticles, because it does not require complex processes, such as liquid–solid separation and washing and drying/annealing, as in wet chemistry methods [51,52,65]. A general schematic of FS is represented in Figure 2. Generally, the process starts from the generation of metal precursor mists or droplets from liquid precursors and/or precursor mixtures by an evaporator/aerosol generator. In another case, a gas-phase precursor generated from liquid precursor using an evaporating method is fed into flame. The common Ti metal precursors are titanium (IV) chloride ($TiCl_4$), titanium isopropoxide (TTIP, $TiC_{12}H_{32}O_4$) and titanium butoxide (TBT, $TiC_{16}H_{36}O_4$). Metal-precursor-containing mists/aerosols are carried by carrier gas (generally N_2 or Ar) together with reaction gas (O_2 or air) into the reaction zone, or high-temperature flame, where the particles are formed. The final particles are collected at the back filters in the collecting system. This process is able to accurately control the synthesis parameters, which enables the tuning of the shapes, sizes, chemical compositions and nanostructures. The particles are generated rapidly and continuously, which is suitable for large-scale production with the purpose of commercialization. FS is flexible for particulate powder production [66,67] or direct thin film depositing/coating [68–70]. The particle formation process in FS is represented in Figure 2b. First, the liquid precursor is evaporated beneath a flame to form the gas-phase precursor. Later, in the high-temperature flame, the gaseous precursor goes through an oxidation reaction or thermal deposition/hydrolysis and nucleates to form nanoclusters. Along the flame, particles grow by aggregation/agglomeration to form the final particle product [53].
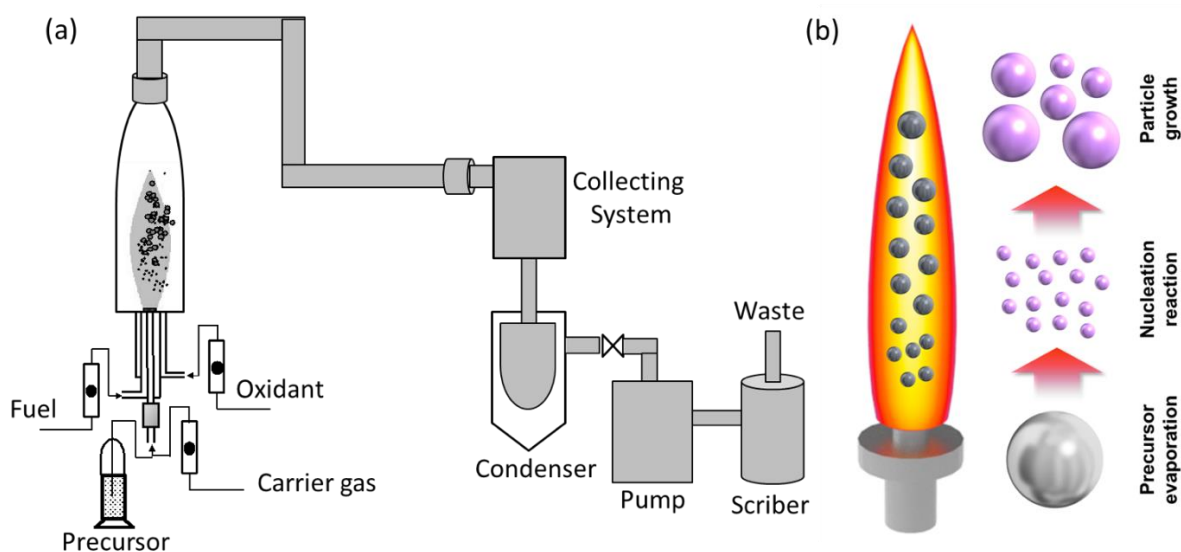
Figure 2. (**a**) General configuration of the flame synthesis; (**b**) particle formation process.

The properties of the FS product can be tuned based on the simple controlling parameters, including the types of precursors, the precursor's feeding rates/methods and the concentrations, reaction temperatures and gas flow rate. The different types of precursors (e.g., TTIP, $TiCl_4$ or TBT) affect the morphological structure, phase and size of the particles [71,72]. In addition, the precursor concentration is considered as an important operational parameter, which greatly impacts on the phases, sizes and structures of the final products. The primary particle sizes generally increase with an increase in the precursor concentration. An increase in the concentration leads to an enhanced nucleation rate and surface reaction [71,73]. In rare cases, an increase in the concentration leads to a decrease in the primary particle size due to the enlarged numbers of nuclei, which revolutionize to form individual particles (surface growth does not occur in this case). Contradictory to the primary particles, the secondary particle sizes always increase with increase in the concentration of the precursor due to the aggregation effects [71,73]. The temperature is a very important parameter for controlling the phases, structures and sizes of the particles because it affects the reaction, nucleation, collision and sintering rate. Generally, an increase in the temperature enhances the rutile formation. The flame is obtained from the combustion of fuel gas (e.g., CH_4, H_2 and C_2H_2) and oxidant (oxygen or air) [74–76]. In the flame reactor, the reaction zone's temperature can be easily controlled by the selection of the fuel/oxidant types and the flow rate of their mixtures. The combustion flame can produce a large amount of heat, up to more than 2200 °C [75]. At this high temperature, a highly crystalline TiO_2 product can be obtained without post-annealing. Binary phases of rutile and anatase are commonly formed, which are considered a target for obtaining high photocatalytic activities [67,72,76,77]. However, it is a large drawback that this high temperature also leads to particle growth by the aggregation/agglomeration of the primary particles to form larger particles (i.e., secondary particles), as in Figure 2b. Therefore, polydispersed sizes of particles are commonly formed with a broad size distribution, ranging from several nanometers to hundreds of nanometers. Figure 3a shows the structure of TiO_2 particles with 3.6% WO_x synthesized from a C_2H_2/O_2 flame. The particles were in the range from 5 to 50 nm [78]. It is very challenging to produce TiO_2 with a unimodal size by the flame method.

Figure 3. TEM images of TiO_2 FS products: (**a**) anatase–rutile with 3.6 mol.% WO_x synthesized by conventional flame synthesis (Re-printed/adapted with permission from Ref. [78]. Copyright 2008, Elsevier); (**b**) mixed phases of anatase–rutile–TiO_2-II synthesized from a laminar premixed stagnation flame (Re-printed/adapted with permission from Ref. [74]. Copyright 2018, American Chemical Society).

Recently, the nonconventional phases of TiO_2, such as (B)-phase or α-PbO_2-type TiO_2 (TiO_2-II), were produced by a laminar premixed stagnation flame of C_2H_2/O_2 from TTIP precursor [74,75]. Wu et al. synthesized mixed phases of anatase, rutile and srilankite (TiO_2-II) by tuning the flame conditions, such as the gas flow rates of fuel, oxygen and argon carrier [74]. Fine particles of 10 to 20 nm were produced from this reactor (see Figure 3b). By using a similar reactor, Manuputty et al. were able to synthesize α-PbO_2-type TiO_2 (TiO_2-II) and other polymorphs, such as anatase, rutile and (B)-phase [75]. It is the first report on this unusual phase because TiO_2-II exists in high-pressure conditions or stabilizes under three-phase heterojunctions of anatase–rutile–TiO_2-II. TiO_2-II/rutile was obtained under oxygen-lean conditions with a high-temperature C_2H_2/O_2 flame (1800–2269 °C). By changing the ratio of oxygen/fuel, different crystallized phases of TiO_2, including anatase, rutile, (B)-phase and TiO_2-II, could be formed. The formation of TiO_2-II in atmospheric pressure in this flame reaction is explained by a kinetics force through the oxidation and solid-state transformation of TiO_x intermediate [75]. Very few cases have generated particles with a hollow-shell structure by introducing additives (e.g., urea, HNO_3 and water content) into the precursor solution, which is explained later in this paper [79,80].

Nanopowder with limited nanostructures is produced from the FS method. Unlike solution-based methods, which can produce a variety of nanostructures, including quantum dots (QDs) and one-dimensional (1D) (e.g., nanotubes, nanorods and nanowires), 2D (e.g., nanosheets and nanoflakes) and 3D structures (e.g., nanoflower, nanospheres and core–shell structures) [81–83], FS allows for the production of only a few structures, such as nanospheres, nanoparticulates or hollow-shell structures. Especially, using FS, it is hard to synthesize very fine particles with a narrow size distribution, because with a high-temperature flame, a particle's growth by aggregation/agglomeration is unavoidable.

3. Defects and Doping

3.1. Native Defects

It is known that native defects, such as oxygen vacancies, Ti^{3+}, Ti^{4+} interstitials and Ti^{4+} anti-sites (Ti^{4+}_O), can lead to changes in the atomic and electronic structures of TiO_2 and influence the photocatalytic activities of TiO_2. In flame synthesis, in situ hydrogenation was developed to induce defects, such as oxygen vacancies and Ti^{3+} doping on the surface of TiO_2 [84,85]. Huo et al. developed an in situ hydrogenation prototype by supplying H_2 gas on the top of the flame inside the chamber by a homemade ring-shaped nozzle with 16 openings (diameter = 1 mm) placed at 15 mm from the nozzle flame of a H_2/O_2 mixture ($H_2/O_2 = 1$) (represented in Figure 4a) [84]. $TiCl_4$ was used as a starting precursor heated to

30 °C. TiCl$_4$ gas was carried by N$_2$ gas and passed through the flame. The TiO$_2$ product was composed of spherical particles with sizes of 20–40 nm, and composite phases of anatase and rutile were obtained in this work. With the in situ hydrogenation, the rutile phase was increased from 8.8% to 31.3 % due to the increase in the temperature by H$_2$ oxidation. The gray/blue color of the produced powder clearly indicated the defect-induced structure of the TiO$_2$, because pristine TiO$_2$ exhibits a white color. From the high-resolution transmission electron microscopy (HR-TEM) images in Figure 4b,c, shells with disordered layer on particle surface are clearly observable [84]. This kind of structure is always obtained with post-synthesis hydrogenation for producing defected TiO$_2$ (termed as black TiO$_2$) [16]. Electron paramagnetic resonance (EPR) spectroscopy and X-ray photoelectron spectroscopy (XPS) analysis confirmed the presence of Ti^{3+} species, the amount of which could be tuned by H$_2$ flow rates (up to 720 L·h^{-1}). Flame-synthesized Ti^{3+}-doped TiO$_2$ was effectively used for photocatalytic methylene-blue degradation under a Xe lamp (>400 nm) [84]. A photoelectrochemical cell (PEC) fabricated from Ti^{3+} self-doped TiO$_2$ generated a high photocurrent density up to 1090 nA·cm^{-2}, while a PEC of pristine TiO$_2$ could generate a photocurrent up to only 428 nA·cm^{-2}. Ti^{3+} created a subenergy level below the conduction band of TiO$_2$, which reduced the bandgap of TiO$_2$, resulting in visible-light absorption. In addition, Ti^{3+} acts as the hole-trap and suppresses the electron–hole recombination. Under visible light radiation, excited electrons residing on the Ti^{3+} state react with dissolved O$_2$ on the particle's surface to form superoxide anions (O$_2$$^{\bullet-}$). At the valence band, holes oxidize water to form hydroxyl radicals (●OH). These superoxide anions (O$_2$$^{\bullet-}$) and hydroxyl radicals (●OH) are further utilized for BM degradation. Table 1 shows the summary of recent works related to defective and heterostructured TiO$_2$ synthesized using FS.
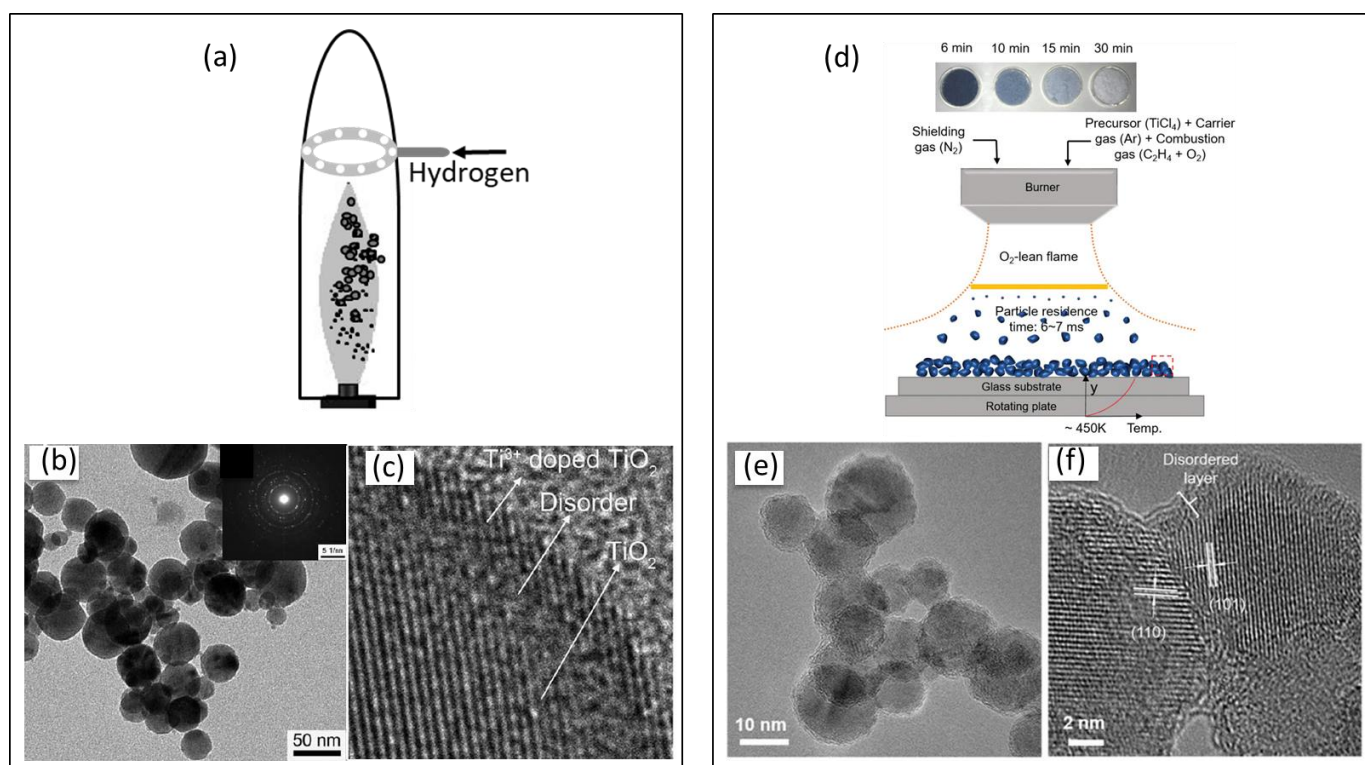
Figure 4. Synthesis of the defected TiO$_2$ prepared by two flame reactors. The in situ hydrogenation reactor: (**a**) reactor setup; (**b**,**c**) TEM and HR-TEM images of powder prepared from the in situ hydrogenation reactor (Re-printed/adapted with permission from Ref. [84]. Copyright 2014, the Royal Chemical Society). Flame stabilized on a rotating surface (FSRS): (**d**) FSRS setup; (**e**,**f**) TEM and HR-TEM images of the formed product at a 6 min deposition time (Re-printed/adapted with permission from Ref. [86]. Copyright 2020, John Wiley and Sons).

Using a flame stabilized on a rotating surface (FSRS), TiO_{2-x} with different kinds of oxygen deficiencies could be synthesized [86]. A mixture of precursor gases of $TiCl_4$/Ar was delivered into the C_2H_4/O_2 flame. A rotating-plate-supported glass substrate was placed at the bottom of the flame for the particle deposition (the experimental setup is summarized in Figure 4d). Under an O_2-lean flame, the oxygen vacancy content and location could be simply controlled by the particle deposition time. At a short deposition time (6 min), defect-rich particles were produced, while the elongation of the deposition time produced TiO_{2-x} with fewer defects. The obtained product was composed of fine spherical particles (10–20 nm) with a major phase of rutile, along with minor phases of anatase and TiO_2-II. At a short deposition time, typically 6 min, defect-rich TiO_{2-x} was simply observed by its blue color (Figure 4d). The TEM/HR-TEM showed the nanostructure of the particles, which was highly crystalline at the core and amorphous/disordered at the shell (Figure 4e,f). By using the temperature programmed oxidation (TPO) method, the location of the oxygen vacancy defects through the particles could be analyzed. At a short deposition time, oxygen vacancies were formed throughout the particles, including both on the surface and in bulk. Since defects are not stable, particularly surface oxygen vacancy defects, the concentration of the defects decreased with the increase in the deposition time due to the oxidation of atmospheric O_2 at the substrate. Due to the high-temperature flame (~2103 °C) on the top of the substrate, the particles underwent thermal sintering after deposition on the substrate, which resulted in the formation of a grain boundary between adjacent nanoparticles. From this work, it was revealed that moderate oxygen vacancies and oxygen vacancies locked at the grain boundary facilitated the anchoring and reduction of the Pt cocatalyst during the photocatalysis reaction. The FSRS-made TiO_{2-x} showed exceptional photocatalysis for H_2 generation under visible light (>400 nm) [86]. The maximum production of H_2 from the methanol solution obtained from using TiO_{2-x} was ~960 $\mu mol \cdot g^{-1} \cdot h^{-1}$, which was 12 times higher than that proceeded by commercial P25. It was proposed that balancing the defects between the surface and bulk was the major factor attributing to this photocatalysis. Typically, a Pt metal cocatalyst (Pt^0) is preferentially deposited at or near the grain boundary, which contains higher electron concentrations. Therefore, defects such as oxygen vacancies at the grain boundary enhanced the reduction of the Pt^{6+} to Pt^0 metal. However, excessive defects might act as a recombination center, which is not beneficial for photocatalysis. That is why at a long deposition time (>15 min), the photocatalytic H_2 production was lower due to the excessive surface oxygen vacancies.

3.2. Impurity Doping

A high temperature in the flame synthesis is beneficial for doping foreign elements into TiO_2 crystals. Post-annealing is generally needed with wet chemical methods (e.g., precipitation) for successful doping. A numbers of works have been reported on doping TiO_2 nanoparticles with metal ions (e.g., V, Cr, Fe, Co, Mn, Mo, Ni, Cu, Y, Ce, Nb, Zr and Mg [67,87–93]) and non-metal ions (e.g., S, N and F [79,94–96]). Doping is very complicated phenomena, which improves or deteriorates the photocatalytic activities of TiO_2. The doping behaviors depend on a dopant's size, valent states and the temperature of the flame.

Table 1. Summary of defective and heterostructured TiO_2 nanoparticles synthesized by FS.

Materials	Precursor/Concentration/ Feeding Rate	Gas	Product's Properties	Photocatalysis	Reference
Ti^{3+}-TiO_2	$TiCl_4$/0.01~0.2 mol·h^{-1}	H_2/O_2/N_2	spherical; sizes (20–40 nm); A-R (A: 68.7%); bandgap (3.07 eV); SSA (42.3 m^2·g^{-1}); production rate~3.2 g·h^{-1}	MB degradation and PEC under visible light (>400 nm); max. photocurrent: 1090 nA·cm^{-2}	[84]
TiO_{2-x}	$TiCl_4$/3 mL·h^{-1}	C_2H_4/O_2/Ar/N_2	spherical; sizes (10–20 nm); A-R-TiO_2-II (R:70%); bandgap (2.8–3 eV); SSA (100–120 m^2·g^{-1})	H_2 generation under visible light (>400 nm) with Pt; max. H_2 rate: 960 $\mu mol \cdot g^{-1} \cdot h^{-1}$	[86]

Table 1. *Cont.*

Materials	Precursor/Concentration/ Feeding Rate	Gas	Product's Properties	Photocatalysis	Reference
M- TiO_2 (M = V, Cr, Fe, Co, Mn, Mo, Ni, Cu, Ce, Y and Zr)	TTIP (0.5M)/vanadium (V) tri-i-propoxy oxide/chromium (III) 2-ethylhexanoate/iron (III) naphthenate/cobalt 2-ethylhexanoate/manganese (III) naphthenate/molybdenum 2-ethylhexanoate/nickel (III) naphthenate/copper (II) 2-ethylhexanoate/zirconyl 2-ethylhexanoate/3 mL·min^{-1}	CH_4/O_2	spherical/particulate; sizes (51–99 nm); A-R (A: 12–80%); bandgap (2.37–3.21 eV); SSA (60–108 m^2·g^{-1})	acetonitrile conversion under visible light; max. rate constant of Cr-doped TiO_2, k: 0.812 m^{-3}·g^{-1}·h^{-1}	[88,89]
N-TiO_2	TTIP-nitric acid-ethanol-DI-urea/ 3 mL·min^{-1}	CH_4/O_2	spherical/particulate; sizes (50–300 nm); A-R (A: 47–66%); bandgap (2.47–2.95 eV); SSA (17–38 m^2·g^{-1})	phenol degradation under visible light	[79,97]
N-TiO_2	TBT-ethanol (0.5M)/NH_3-H_2O (28 wt.%, 2 mL·min^{-1})/5 mL·min^{-1}	H_2/Air/N_2	spherical; sizes (10–30 mn); A-R (A: 90.8%); bandgap (2.90 eV); SSA (45.1 m^2·g^{-1});	N/A	[98]
S-TiO_2	TTIP-sulfuric acid-ethanol-DI (0.3M)/3 mL·min^{-1}	CH_4/O_2	spherical; sizes (75–311 nm); A-R (A: 59–66%); bandgap 2.78–2.94 eV; SSA (5–13 m^2·g^{-1});	acetaldehyde degradation under visible light	[95]
F-TiO_2	TTIP -propionic acid-xylene/ hexafluorobenzene/4 mL·min^{-1}	CH_4/O_2	A-R (A: 86–91%); SSA (113–117 m^2·g^{-1}); UV-vis abs < 400 nm	degradation of FA and TAOH under UV-light (>340 nm); max. rate constant k$^0_{FA}$: 1.89 × 10^{-7} M·s^{-1}, k$^0_{TAOH}$: 14 nM·s^{-1}	[94]
Pt/TO_2	BTB-ethanol/platinum acetylacetonate/3 mL·min^{-1}	CH_4/O_2/Ar	particulate; size (~10 nm); A-R (A: 83–89%); SSA (167 m^2·g^{-1}); bandgap (3.07–3.19 eV);	H_2 production under Xe lamp (300 W), max. H_2-rate: 552.39 μmol·h^{-1}	[99]
Pt/TiO_x	TTP/platinum acetylacetonate-xylene-acetonitrile/0.4 L·min^{-1} (N_2 flow)	$CH_4/O_2/N_2/H_2$	particulate; size (20–50 nm); A-R (A: 69%); SSA (74 m^2·g^{-1}); bandgap (2.88 eV)	CO_2 reduction under Xe lamp; max. AQY: 1.49%, CH_4 selectivity: 81%	[85]
Pt/N-TiO_2	TBT-ethanol/chloroplatinic acid/ 5 mL·min^{-1}	$H_2/O_2/N_2/NH_3$	particulate; size (10–25 nm); A-R (A: 70.86%); SSA (61.4 m^2·g^{-1});	N/A	[76]
Pt/F-TiO_2	TTIP-propionic acid-xylene (0.6 M)/hexafluorobenzene/ hexachloroplatinic acid hydrate/4 mL·min^{-1}	CH_4/O_2	A-R (A: 86–91%); SSA (130–142 m^2·g^{-1}); UV-vis abs < 400 nm	methanol steam-reforming under UV-light (>350 nm); max. H_2 rate: 22 mmol·h^{-1}·g^{-1}	[100]
Pd/TiO_2	TTIP-ethylhexanoic-acetonitrile (0.159 M)/Pd-acetylacetonate/ 8 mL·min^{-1}	CH_4/O_2	spherical/particulate; size (11–17 nm); A-R-amorphous (A: 74–86%); SSA (85–116); UV-vis abs < 550 nm	NO removal under solar light; max. NO removal: 67% after 5-h reaction	[101,102]
Au/TiO_2	TTIP-xelene-pyridine (0.15 M)/1 % dimethyl-gold (III)-acetylacetonate/3.1 mL·min^{-1}	CH_4/O_2	spherical/particulate; size (10–500 nm); A-R (A: 90 wt.%); size (10–500 nm); SSA (106 m^2·g^{-1})	water-splitting reaction under Hg lamp (330–450 nm); max. H_2 rate: 52 μmol·h^{-1}·g^{-1}	[103]
AuPd/TiO_2	TTIP-xylene-acetonitrile (0.5 M)/gold chlorite hydrate/palladium acetylacetonate/5 mL·min^{-1}	CH_4/O_2	spherical/particulate; size (10–30 nm); A-R (major A); SSA (99–152 m^2·g^{-1})	N/A	[104]
AuPt/TiO_2	TBT-xylene-ethanol (0.05 mol.)/chloroplatinic acid hexahydrate/chloroauric/5 mL·min^{-1}	H_2/O_2	spherical/particulate; size (20–30 nm); A-R (major A); SSA (58–78 m^2·g^{-1})	N/A	[105]
Cu/TiO_2	TBT-ethanol/ Cu(NO_3)$_2$.3H_2O/5 mL·min^{-1}	CH_4/O_2	spherical; A-R (A 90–80%); size (~10 nm); bandgap (3.09–3.15 eV); SSA (94–106 m^2·g^{-1})	CO_2 reduction under Xe lamp (300–400 nm); max. AQY$_{CH4}$: 0.087% and AQY$_{CO}$: 0.057%	[106]
CoPt/TiO_2	TBT-ethanol/Co(NO_3)$_2$.6H_2O/ 5 mL·min^{-1}	H_2/O_2	spherical/particulate; size (5–25 nm); A-R (A 69.7%); size (5~25 nm); SSA (60.2 m^2·g^{-1})	N/A	[107]

Metal doping: Inturi et al. reported a wide range of metal ion doping into FS-made TiO$_2$ by feeding a mixed TTIP precursor solution into a CH$_4$/O$_2$ flame [87–89]. TTIP and metal ion precursors were dissolved in o-xylene/acetonitrile as a solvent to achieve a total concentration of 0.5 M. Metal precursors, such as chromium (III) 2-ethylhexanoate, vanadium (V) tri-i-propoxy oxide, iron (III) naphthenate, manganese (III) naphthenate, nickel (III) naphthenate, copper (II) 2-ethylhexanoate, cobalt 2-ethylhexanoate, molybdenum 2-ethylhexanoate, zirconyl 2-ethylhexanoate and yttrium (III) naphthenate, were selected for Cr, V, Fe, Mn, Ni, Cu, Co, Mo, Zr and Y doping, respectively. The doping concentration was fixed to 5% (M/Ti = 0.05). In general, doping with these metals promoted rutile phase formation. Among these metal dopants, Co and Ni induced the highest fraction of rutile phase (84 and 88%), while undoped TiO$_2$ contained only ~19% rutile [88]. It is commonly known that doping induces defects, such as oxygen vacancies or Ti^{3+} species, which should be an important nucleation center for rutile phase formation [77]. Therefore, the rutile phase increased with the increase in the doping contents. In addition to a phase change, a change in the bandgap of the TiO$_2$ was also observed with some metal dopants. A bandgap reduction was observed with Co, Cr, Cu, Fe, Mn, Ni and V doping. The undoped TiO$_2$ had a bandgap energy in the UV range, 3.08 eV. Ni doping induced the smallest bandgap of TiO$_2$ (2.37 eV). However, some of the other metal dopants, such as Zn, Y, Mo and Ce, enlarged the bandgap of TiO$_2$. These changes in the bandgap energies indicate that the doping behaviors were different from the individual metal ions. Some elements with ionic sizes similar to or smaller than a Ti^{4+} ion, such as Cr, Fe, Co, Mn, Ni, Mo, V, Cu and Zr, are more likely to be doped into crystal lattices of TiO$_2$ (interstitial doping and/or substitutional doping). Some elements with bigger ionic sizes than Ti^{4+} ions, such as Y and Ce, preferentially formed as metal oxides dispersed on the surface of TiO$_2$. However, in Inturi's work, the metal oxide-related phases were not detected by the XRD analysis [88], which might be due to the lower content of the doping concentrations. The photocatalytic activity of the synthesized materials was evaluated by acetonitrile degradation under visible light. Although some dopants reduced the bandgap of TiO$_2$, which resulted in visible light absorption, not all of them improved the photocatalytic activities of TiO$_2$ in visible light. Only three dopants (Cr, Fe and V) enhanced the visible-light photocatalytic activities of the acetonitrile degradation. Among them, Cr doping showed the highest photocatalytic activities of the acetonitrile conversion due to the fact of its strong interaction between of the Cr–O–Ti bond [88,89]. The maximum decay constant of acetonitrile degradation was $K_A = 0.812$ m^3·g^{-1}·s^{-1} [89]. Doping Cr ions induced a substantial amount of Ti^{3+}, which might account for the improving visible light photocatalysis [108–112]. The maximum Ti^{3+} concentration was up to Ti^{3+}/Ti^{4+} = 1.14 at Ti/Cr = 40 [88,89]. The synchronization of the Cr ions and TiO$_2$ activated the visible light photocatalytic activities [108–112]. The Cr^{6+} species was the most active species in the Cr-doped TiO$_2$, because the synchronization of Cr^{6+} and TiO$_2$ took place by the Cr^{6+} = O^{2-} → Cr^{5+}–O^{1-} route, which is responsible for the visible light photocatalytic reaction [89,108].

In the Ce-doping case, Inturi et al. reported that the bandgap of TiO$_2$ increased (3.08 vs. 3.13 eV), and the photocatalytic degradation of acetonitrile under UV radiation was reduced [88]. However, other works conducted by Mikaeili et al. [67] and Chaisuk et al. [113] showed different results, where the bandgap was reduced by the Ce doping, and the photocatalytic degradation of methylene blue under visible light (>400 nm) also increased. Both Mikaeili and Chaisuk observed the existence of CeO$_2$, even at low doping concentration (3~5 at.%), while Inturi did not. This complicated phenomenon of the Ce-doping system was probably due to the fact of its unusual redox shift (Ce^{4+}<–>Ce^{3+}) [89]. Because the ionic size of Ce (Ce^{4+} = 101 pm; Ce^{3+} = 115 pm) is larger than Ti (Ti^{4+} = 74.5 pm; Ti^{3+} = 81 pm), it is hard to dope Ce ions into a TiO$_2$ lattice. However, it is possibly formed as a solid solution and composite (e.g., CeTi$_2$O$_6$ [114] and CeO$_2$-TiO$_2$ [115]). In an oxidative atmosphere, CeO$_2$-TiO$_2$ was stable, while in reductive atmospheres, other phases, such as Ce$_2$O$_3$·4TiO$_2$ and Ce$_2$O$_3$·2TiO$_2$, were reported [115]. In flame synthesis, the presence of CeO$_2$ was observed in the rutile phase only. Because

of its larger radius, cerium was ejected outside the crystal lattice of the TiO_2 rutile and nucleated on the surface as CeO_2 clusters, later forming CeO_2 nanoparticles [114]. The existence of brannerite ($CeTi_2O_6$) at the interface of CeO_2 and TiO_2 is a typical characteristic of flame-made products. Brannerite is high-temperature entropy-stabilized compound, which is synthesized at a high temperature and subsequent quenching. A flame reactor is characterized by the suitable conditions of both high temperature and quenching process, which allow to obtain the brannerite phase. The formation of brannerite stabilizes oxygen vacancies at the interfaces of CeO_2-TiO_2 due to the existence of Ce^{3+} in the brannerite. Furthermore, the incorporation of Ce^{3+} into the TiO_2 lattice induces oxygen vacancies due to the charge compensation of Ce^{3+} and Ti^{4+}, which enhances the rutile–anatase transformation [114]. Doping with Ce varies the band structures of TiO_2 depending on the doping concentrations, which alter the photocatalytic activities of TiO_2 [115]. In terms of heterogeneous catalysis, such as CO oxidation [116] and NO_x reduction [114], CeO_x-TiO_2 always shows a better performance due to the Ce-Ti-O interactions at the interface.

Non-metal doping: Anion doping is generally used to modify the valence band of TiO_2 for narrowing the bandgap. In contrast to cation doping, anion doping does not play the role of charge carriers and recombination center, which minimizes the side effects on photocatalysis. Only a few works have reported anion doping (e.g., N, S and F-doping) by flame synthesis.

N doping has been extensively studied for improving the visible light photocatalysis of TiO_2. However, the doping sites of N altered the photocatalytic activities of TiO_2 [117,118]. In flame synthesis, N doping was obtained by introducing nitrogen sources (e.g., urea and nitric acid) into the Ti-precursor solution [79,80,119] or supplying a NH_3 solution into the flame chamber [77,98]. Nitrogen-containing materials, such as aqueous solutions of nitric acid and urea, were premixed with a Ti-precursor solution [79,80,97,119] and sprayed into the flame nozzle. The precursor solution was simply prepared by dissolving TTIP into dilute nitric acid followed by the addition of water/ethanol and urea [79]. The amount of the N-doping concentration did not alter much with the increase in the nitric acid concentration. From the XPS analysis, the N-doping concentration merely increased from 0.11 at.% to 0.13 at.% with the increase in the nitric acid concentration from 0.8 to 3 M, respectively [80]. In addition, the bandgap of TiO_2 was slightly reduced from 3.12 (pristine state) to 2.95 eV upon the addition of 3 M nitric acid. It was expected that the majority of the nitric acid was oxidized in the flame to N_2, resulting in the limitation of the nitrogen-doping concentration. However, when the secondary N-source urea was added, the N concentration increased from 0.20 at.% to 1.63 at.% with the increase in the urea concentration from 0.25 to 2 M, and the bandgap largely decreased to 2.51 eV (at 2 M urea) [80]. Urea was thermally decomposed to NH_3 and reacted with an oxygen functional group of TiO_2, which subsequently formed intermediates resulting from ammonia pyrolysis (e.g., N, NH, NH_2 and N_2H_x, x = 1–4). These intermediates would react with TiO_2 to form N-doped TiO_2. Both substitutional and interstitial doping was observed in this preparation method. However, the addition of secondary N-source urea increased the interstitial N doping based on the XPS deconvoluting data [119]. In addition to changing the optical bandgap of TiO_2, the addition of nitric acid and urea suppressed the formation of anatase, where the percentage of anatase decreased from 82% in the undoped TiO_2 to 62% and 59% with the addition of 1 M nitric acid and 1 M nitric acid + 1 M urea [119]. The enhanced rutile phase formation with the addition of nitric acid and urea should be attributed to defect formation (e.g., oxygen vacancies) due to the N-doping effects and increased flame temperature due to the presence of additional organics, such nitric acid and urea, which acted as fuels.

The effects of the addition of HNO_3 and urea on the morphologies and nanostructures are depicted in Figure 5a,b, from Reference [95]. Without the addition of a nitrogen source, the TiO_2 particles were small (<20 nm). The addition of nitrogen sources, such as HNO_3 and urea, produced large spherical particles with sizes ranging from 30 to 150 nm with a hollow-shell structure. This hollow-shell structure formed from the low enthalpy flame

due to the addition of N-containing sources, such as urea and HNO_3/water, which resulted in the enhanced precipitation of the reaction/intradroplet reaction [79,80,97,119]. The selected area electron diffractions of the corresponding particles informed the polycrystalline nature, and were indexed to the anatase and rutile phases. The inset in each figure shows images of TiO_2 powder with and without HNO_3-urea. The color of the TiO_2 powder changed from white to yellowish with HNO_3 and HNO_3-urea, inferring the rich N doping with urea as a secondary N-doping source. The optical absorption in the visible range was also enhanced with the addition of urea. From the same research group, it was also revealed that the addition of water improved the visible-light absorption of the N-doped TiO_2 (see the absorption spectra in Figure 5c) [79]. The nitrogen-doping concentration was increased from 0.43 at.% to 0.96 at.% when the water content was increased from 25 to 50%. Therefore, the addition of water improved the visible absorption of TiO_2, which demonstrates its potential as a photocatalyst candidate for solar harvesting. Alternatively, N doping was also prepared by spraying a NH_3/water solution onto the top of the flame, which allowed for the formation of N-surface-doped TiO_2 [76,98]. Figure 5d shows that a NH_3 aqueous solution was supplied on the top of the flame, and the generated TiO_2 nanoparticles were treated with NH_3 molecules and formed surface N-doped TiO_2, where the yellowish color of the powder indicated successful N doping. This procedure is similar to N doping prepared by the conventional NH_3-annealing method [98]. N doping was dominant in the interstitial sites at the surface of the TiO_2 particles. The photocatalytic degradation of phenol under visible light (>420 nm) was studied to evaluate the photocatalytic activity of newly synthesized N-doped TiO_2. The 500 ppm phenol was significantly degraded within a 2 h reaction by N-doped TiO_2, while pristine TiO_2 showed negligible phenol degradation. Typically, when a secondary N source of urea was added, the photodegradation of phenol also increased, which indicates that the photocatalytic activity of N-TiO_2 under visible light was affected by the N-doping concentration. The dominant factor for the enhanced photocatalytic activities under visible light should be due to the reduced band gap energy of TiO_2 by incorporating a N atom into the TiO_2 lattice, resulting in the alteration of the electronic band structure. The N doping creates a mid-gap energy state of N *2p* formed above the O *2p* valence band and narrows the band gap of TiO_2 from 3.07 to 2.47 eV [97].

S doping: S element was successfully doped to TiO_2 material using one-step FS with TTIP and sulfuric acid as Ti and S precursors [95]. It was suggested that the preparation of the titanium oxysulfate precursor allowed for the S doping into the TiO_2 framework. The titanium oxysulfate precursor was prepared by mixing TTIP in water to form white precipitate. This precipitate was redissolved by the addition of sulfuric acid. The TTIP-water-sulfuric acid mixture was diluted into ethanol to form the FS precursor. The S-doping amount was controlled by the sulfuric acid concentration. Increasing the sulfuric concentration enhanced the S doping and the rutile phase formation. The percentage of the rutile phase increased from 19% to 34% upon the addition of 1 M sulfuric acid. A further increase in the sulfuric acid above 1 M slightly increased the rutile phase. The maximum doping concentration of S was 8.9 at.% with the addition of 2 M sulfuric acid. The major S species doped into TiO_2 were S^{6+} and S^{4+}, as analyzed by XPS. S^{6+} doping was considered as the major factor for enhancing visible light utilization by inducing mid-energy level below the conduction band of TiO_2, which led to smaller bandgaps. Flame-made S-doped TiO_2 was utilized for acetaldehyde removal under visible light irradiation. The pristine TiO_2, as a control, showed inactivity for acetaldehyde degradation under visible light due to its large bandgap. The photodegradation of acetaldehyde was significantly improved with the S-doping concentration. The following factors may have affected the photocatalytic activity of the S-doped TiO_2: (1) a reduction in the bandgap by the formation of mid-gap energy levels induced by S^{6+} doping under a Ti *3d* conduction band, which resulted in enhanced visible light absorption; (2) lattice defects formed by S doping enhanced the hydroxyl ion absorption and rapid generation of hydroxyl radicals, which are strong oxidation species; (3) formation of Ti-O-S bonds inhibit electron transition and reduce the electron–hole recombination, resulting in high photocatalytic activity [95].
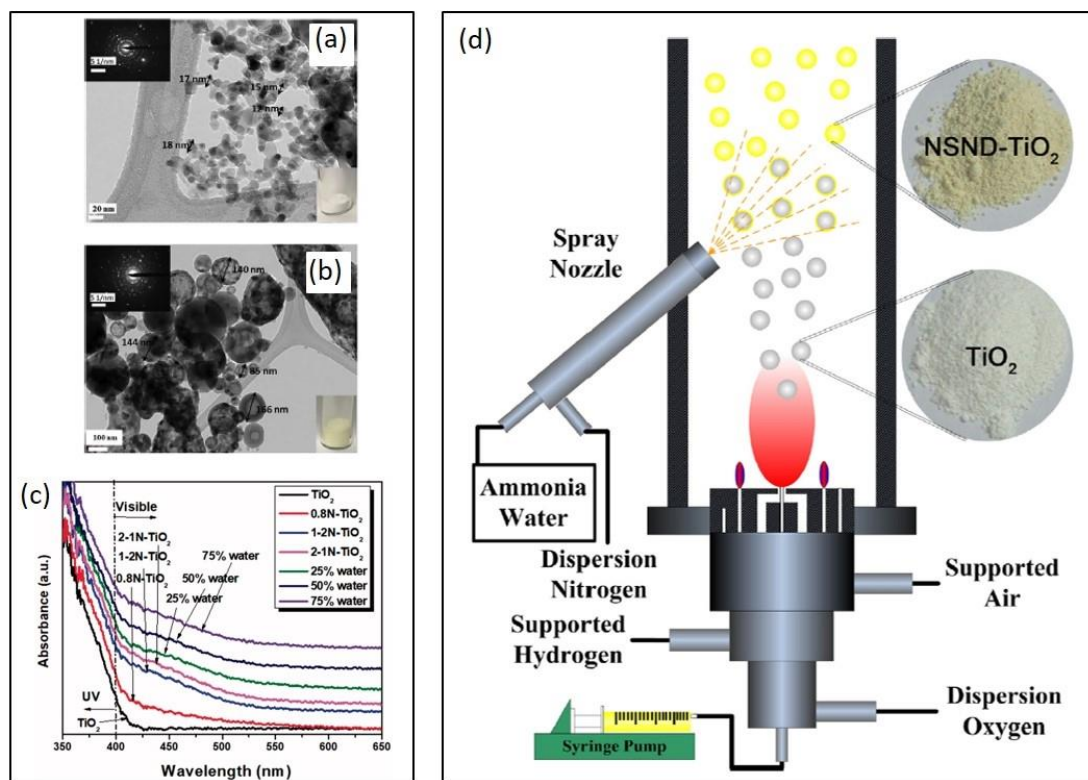
Figure 5. N-doped TiO$_2$ synthesized by mixing N-contained materials with Ti precursor and by supplying NH$_3$ solution into the flame chamber. TEM and digital camera images of TiO$_2$: (**a**) pristine TiO$_2$; (**b**) 1 M HNO$_3$-1M urea (Re-printed/adapted with permission from Ref. [97]. Copyright 2018 Elsevier). (**c**) Effects of the addition of water on UV-vis absorption spectra of N-doped TiO$_2$ (Reprinted/adapted with permission from Ref. [79]. Copyright 2018, Taylor & Francis). (**d**) FS setup for N-doped TiO$_2$ synthesized by NH$_3$ spray and images of the undoped and N-doped TiO$_2$ powder (Re-printed/adapted with permission from Ref. [98]. Copyright 2014, Elsevier).

F doping: F doping was carried out by mixing F sources (e.g., hexafluorobenzene (C$_6$F$_6$)) into a Ti precursor and spraying into the flame reactor [94,100]. The surface area of the obtained F-doped TiO$_2$ did not vary with the changes in the amount of the F source, which indicates that the morphological structures of F-doped TiO$_2$ were not much different from undoped TiO$_2$. However, F doping prohibited the rutile phase formation, which can be attributed to the inhibited condensation of spiral chains of the rutile TiO$_6$ octahedral at a high temperature [94]. The optical absorption revealed that F doping did not have an effect on changing the UV-vis absorption spectra; the UV-vis absorption spectra of both F-doped and undoped TiO$_2$ were <400 nm, which are typical spectra corresponding to the rutile–anatase mixed phase. It is already known that F doping creates new localized levels composed of F *2p* states below the VB of TiO$_2$, but without inducing any variation in the optical absorption. The photocatalytic activity was evaluated by the formic acid degradation under UV light (>340 nm), but the degradation efficiency deteriorated with F doping. Physically absorbed fluorine ions hampered the absorption of formate anions on the surface of the catalyst, typically in an acidic condition, which resulted in the lower photocatalytic degradation of formic acid. However, the photocatalytic conversion of terephthalic acid (TA) into 2-hydroxyl-terephthalic acid (TAOH) increased with F doping, because fluorine ions can be replaced by hydroxyl group at a basic condition, which facilitated the photocatalytic oxidation [94].

4. Heterostructure

Based on the feeding methods of precursors, FS is considered a very promising strategy for the synthesis of multicomponent TiO_2-based compounds composited with other materials within a single step. Generally, multimetal precursors are premixed and sprayed/evaporated into a single flame (Figure 6a). To ensure a homogeneous solution of the mixed precursors, the selection of the types of metal precursors and the precursor's solvents is very important. This feeding method is very facile, but there are some drawbacks to the method, as follows: Unintentional doping will possibly form and change the properties of the synthesized materials. The coverage of the active sites by the inactive phase of the secondary materials is also a main drawback in using premixed precursors. For example, active metal nanoparticles can be covered by TiO_2, which reduces the catalytic activities. Another method is the separate feeding of metal precursors into the same flame or a different flame (Figure 6b,c). These methods can minimize the alloy formation (and/or doping), and they are more promising in terms of synthesizing multicomponent nanoparticles and the facile control of individual components [86,104]. These feeding methods were successfully used to load metal/oxide nanoparticles onto TiO_2 [102,104].
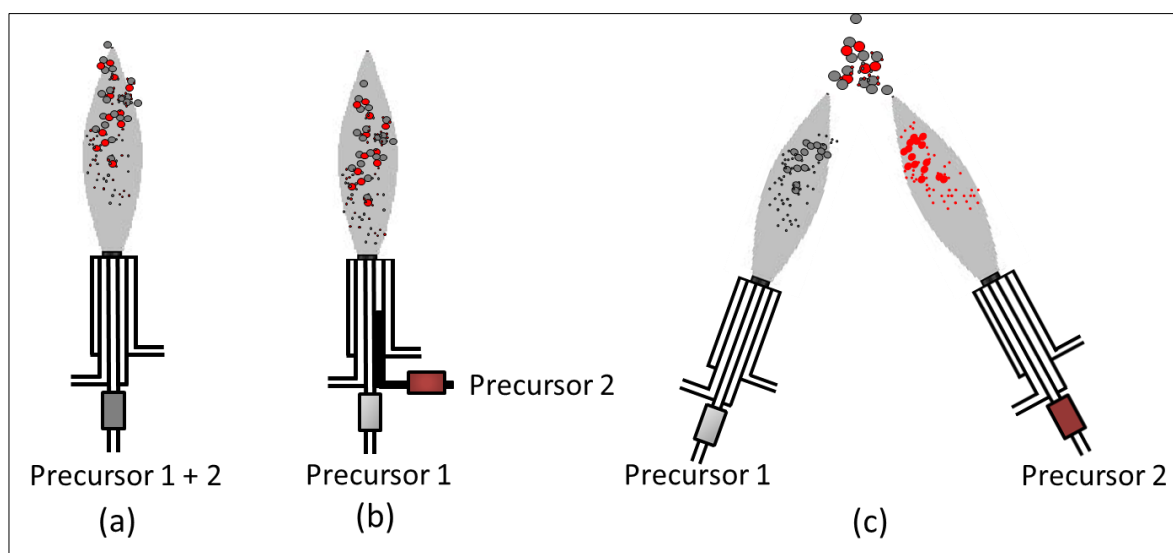

Figure 6. Feeding methods for the synthesis of composite materials by FS: (**a**) all precursors are mixed and fed together; (**b**) precursors are fed separately into different pots of the same nozzle (burner); (**c**) precursors are fed separately into different nozzles.

4.1. TiO_2/Noble Metals/Oxides

Numerous works have reported using nanocomposites of TiO_2 with noble metals and metal oxides, such as Pt/TiO_2 [76,85,100,107,120,121], Pd/TiO_2 [65,101,102,122–124] and Au/TiO_2 [104,125].

Pt loading: FS was applied to load a Pt single atom, nanocluster or nanoparticle onto a TiO_2 support. In most cases, platinum acetylacetonate ($C_{10}H_{14}O_4Pt$) and platinum chloride hexahydrate ($H_2PtCl_6 \cdot 6H_2O$) were used as the Pt metal precursor mixed with TTIP or TBT. The Pt precursor and Ti precursor were premixed as a binary metal feeding solution and sprayed into a single flame [99,126–129]. In some cases, the Pt precursors were fed separately by a sublimation unit into the same flame [130]. Gao et al. synthesized single-atom Pt catalysts anchored to a TiO_2 support at an ultralow concentration (<0.1 at.%), which is very important for activating the H_2 evolution reaction [99]. Due to the difference in the boiling points of PtO_2 and TiO_2 (450 vs. 2727 °C), in hot temperature of the flame (close to the burner), PtO_2 formed as a gas phase surrounding the TiO_2 nanoparticles. Downstream at a lower temperature, PtO_2 condensed onto the TiO_2 surface as a single atom and/or nanoclusters. It was observed that the Pt nanoclusters and nanoparticles were

preferentially formed at a higher concentration (Figure 7b,c). At an ultralow concentration, premixed Pt precursor does not affect phase or bandgap energy of TiO_2. A good dispersion of Pt onto TiO_2 nanoparticles was achieved at both conditions. The Pt-loaded TiO_2 exhibited outstanding photocatalytic H_2 generation, with a production rate up to 552.39 $\mu mol \cdot h^{-1}$, which was 107.5 times higher than the H_2 generated by P25 [99]. The FS enabled the loading of Pt metal at an ultralow concentration as well as well-dispersed single-atom Pt onto the surface of the TiO_2, which was mainly attributed to this extremely high H_2 evolution reaction. Moreover, the FS-made Pt/TiO_2 can potentially be utilized for various catalytic reactions, such as the mineralization of organic matters [127,129], catalytic hydrogenation of 3-nitrostyrene [126], SO_2 oxidation [130] and gas sensors [128].
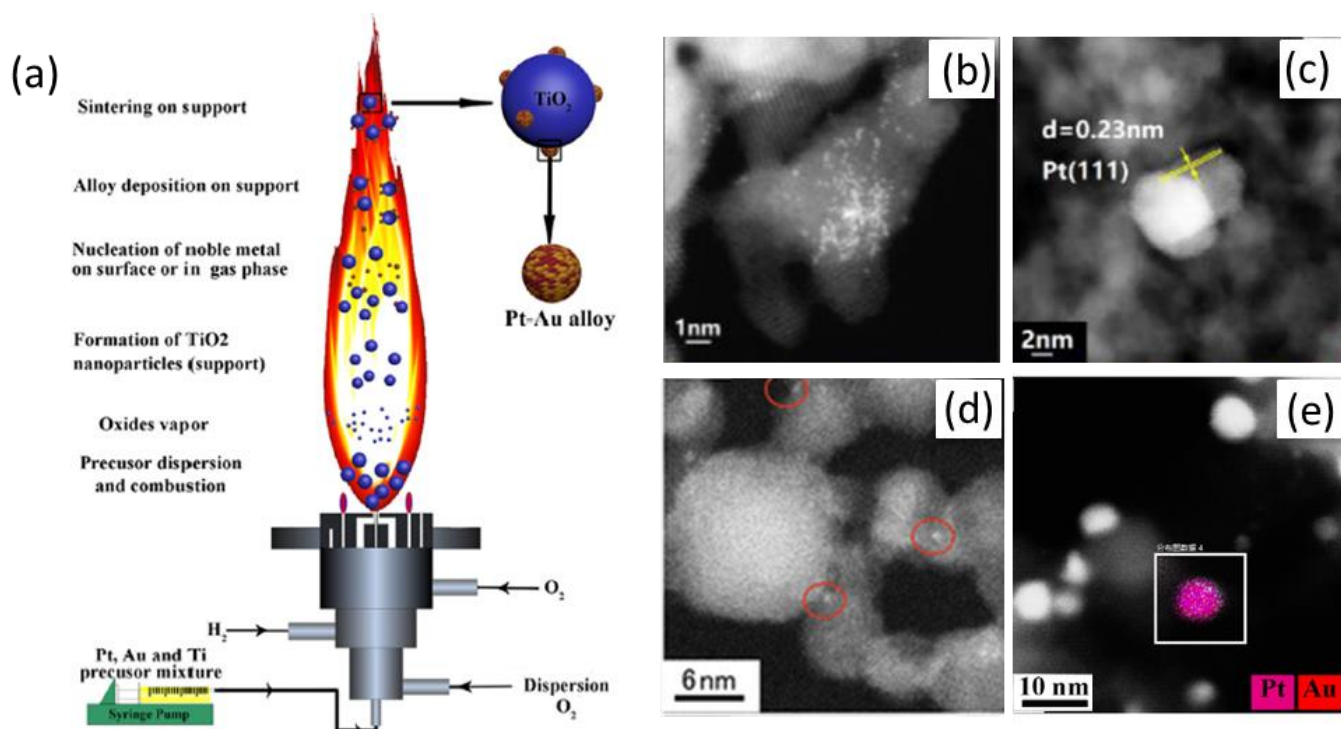
Figure 7. (**a**) Schematics of Pt-Au/TiO_2 formation in FS (Re-printed/adapted with permission from Ref. [105]. Copyright 2020, Elsevier); (**b**,**c**) S/TEM images of Pt-loaded TiO_2 at low and high concentrations (Re-printed/adapted with permission from Ref. [99]. Copyright 2021, Elsevier); (**d**) S/TEM image of Pd-loaded TiO_2, red cycles indicate Pd particles (white spots) (Re-printed/adapted with permission from Ref. [101]. Copyright 2016, American Chemical Society); (**e**) S/TEM image of Pt-Au/TiO_2 and EDS elemental mapping of Pt and Au (inside the white square) (Re-printed/adapted with permission from Ref. [105]. Copyright 2020, Elsevier).

Attempts to use FS to produce more complex structures of TiO_2 by co-inducing defects with Pt/TiO_2 heterostructures have also been successfully reported. The effects of surface-oxygen vacancies on heterostructures of Pt-supported TiO_2 nanoparticles were studied by in situ hydrogenation into flame chambers [85]. Lin et al. invented an in situ hydrogenation system. H_2 gas was supplied by a ring-shaped pipe into the flame chamber in order to provide a reducing atmosphere for inducing the surface oxygen vacancies onto TiO_2 nanoparticles [85]. The Ti-precursor vapor was carried by N_2, while the Pt precursor was separately sprayed into the same flame, which resulted in the formation of a Pt/TiO_2 composite. These composite nanoparticles passed through hydrogenation zone at the top of the flame, leading to the formation of Pt/TiO_2-V_o complex. Oxygen vacancies were successfully induced on the surface of TiO_2 supports and enhanced charge-transfer to Pt nanoparticles, which enhanced the photocatalytic properties for the CO_2 reduction. The electronic metal–support interaction also prevented the loss of metallic Pt^0 and oxygen

vacancies, which improved the lifetime of the catalyst. With a similar concept, a N-doped Pt/TiO_2 complex was synthesized by introducing a NH_3/water solution into the top of the flame [76]. This in situ N-doping procedure was also used to synthesize a composite of Pt/TiO_2 heterostructures, which showed high catalytic CO oxidation and high thermal stability due to Pt-N bond formation. F-doped Pt/TiO_2 was simply produced by mixing all metal precursors (TTIP, hexachloroplatinic acid hydrate, propionic acid and xylene) with a F source of hexafluorobenzene and sprayed into a single flame [100]. The F doping by substitution of the O sites stabilized the metal phase of Pt in the FS. F-TiO_2/Pt increased the hydroxyl moieties on the surface of the TiO_2, which resulted in higher photocatalytic activities of methanol stream-reforming to produce H_2 and CO_2. The maximum H_2 and CO_2 generation from the optimized samples were 22 and 3.3 mmol·g^{-1}·h^{-1}. At lower F doping (<10 at.%), a rich surface of hydroxyl moieties led to an indirect hydroxyl mediated mechanism, which was more selective toward the complete oxidation of methanol to CO_2 and generated H_2. However, at a higher F-doping concentration (>10 at.%), the increase in bulk defects, which acted as an electron–hole recombination center, could reduce the photocatalytic activity [100].

Pd loading: Fujiwara et al. synthesized Pd single-atom-, sub-nanocluster- and nanoparticle-supported TiO_2 composites from a solution precursor of 2-ethylhexanoic acid, acetonitrile, TTIP and palladium acetylacetonate in a CH_4/O_2 flame [101,102,122]. Sub-nanoclusters of Pd (<1 nm) were well distributed on the TiO_2 nanoparticles (see Figure 7d). In FS, substantial oxygen vacancies on the surface of TiO_2 play an important role in stabilizing the Pd nanoclusters. The interaction of the oxygen vacancies and Pd on the FS-made TiO_2 created an intermediate state between the metal and PdO. The Pd sub-nanoclusters were highly stable and resistant to thermal annealing up to 600 °C for 2 h [101]. In later reports, Fujiwara investigated the single atom of Pd-supported TiO_2 using the same synthesis procedure [102,122]. Isolated Pd atoms were observed with an ultralow concentration (<0.1 wt.%), while at a higher concentration, nanoclusters were preferentially formed. Isolated Pd atoms were shown to have higher activities for photocatalytic NO_x removal under solar light than that of the nanoclusters. Within only a 5 h reaction, 67% of the NO_x was decomposed when 1 wt.% Pd-TiO_2 was used, which is much higher than that degraded by commercial P25. The richness of surface defects on the FS-made TiO_2 anchoring the sub nanosized Pd was considered to be the main contribution to the high photocatalytic NO_x removal [101]. Different from Pt, the fact that Pd and TiO_2 have similar boiling points provides the possibility of Pd doping into TiO_2. However, Pd doping into TiO_2 had a minor impact on the photocatalytic activities in these studies [102,122].

Some other works focused on Pd-nanoparticle-anchored TiO_2 [123,124]. By using a similar FS system to Fujiwara [102,122], Mekasuwandumrong et al. obtained nanosized Pd (2–5 nm) decorated on TiO_2 nanospheres, which exhibited excellent catalytic activity for the hydrogenation of heptyne, with a high selectivity of heptane (>90%) [123]. Zong et al. used a stagnation swirl flame (SSF) with an ultrafine spray to produce Pd-nanoparticle-(<2.5 nm)-supported TiO_2 (7–8 nm) [124]. A typical feature of the obtained products from the SSF was a high specific surface area (210–220 m^2·g^{-1}) due to its short residence time and fast quenching, which enabled the generation of very fine particles and a nonaggregated structure. The SSF-made Pd/TiO_2 was utilized for the combustion of CH_4, and it showed high catalytic activity at a low temperature (T_{20} = 293 °C), and the optimized loading concentration of Pd was 15 wt.% [124].

Au loading: Au nanoparticles are among the active noble cocatalysts, and they can be loaded onto TiO_2 nanoparticles for various catalytic reactions. Mädler et al. used gold (III) chloride hydrate as a precursor for gold nanoparticles [125]. Gold precursor was mixed with Ti precursor (TTIP/Xylene) and sprayed into a CH_4/O_2 flame. The sizes of the Au nanoparticles formed varied with the change in the Au precursor concentration; the crystal size of the Au nanoparticles increased from 3.8 to 14.8 nm when the precursor concentration rose from 1 to 4 wt.%. However, the particle structure and crystal phase of TiO_2 were not affected by the addition of Au nanoparticles. It was proposed that

the Au nanoparticles formed by heterogenous nucleation on the metal oxide support or homogenous nucleation of the gold itself [125]. In later work, Chiarello et al. premixed gold precursor (dimethyl-gold(III)-acetylacetonate) into TTIP/Xylene/pyridine solution as a precursor feed [103]. A mixed phase of rutile and anatase (90%) was produced with bimodal sizes, ranging from 100 to ~500 nm for the large spherical particles and 10 nm for the small particles. Au nanoparticles with an average particle size of 2 nm were well dispersed onto the TiO_2 nanoparticles. The FS-synthesized Au/TiO_2 showed its highly active photocatalytic activities for H_2 generation from pure water and methanol solution. The H_2 production rate from water and methanol solution was 52 and 7890 $\mu mol \cdot h^{-1} \cdot g^{-1}$, respectively. These production rates were superior to those obtained from P25/Au, which was prepared from solution method as a comparison sample [103]. By using a similar process for the single-step FS, Au-loaded TiO_2 was reported as an active catalyst for H_2 sensor application [131].

In addition to single loading, the co-loading of Au with other metals was also made possible using FS. Pongthawornsakun et al. studied various feeding methods to prepare Pd-Au-loaded TiO_2 nanoparticles by mix feeding and separate feeding with different compositions, such as $PdAu/TiO_2$, Pd/TiO_2 + Au, Au/TiO_2 + Pd, TiO_2 + AuPd and Au/TiO_2 + Pd/TiO_2 [104]. It was found that there was no significant difference in the TiO_2 structure of all samples in terms of the sizes and surface areas using cofeeding methods. In the prepared nanoparticles, the metallic nanoparticles were well distributed onto the TiO_2 supports. Among the feeding methods, the TiO_2 + AuPd composite catalyst produced by the two-nozzle FSP showed the highest photocatalytic activities of acetylene conversion with 50% efficiency and an ethylene selectivity greater than 95%. The possibility of bimetallic particles can be reduced by separate feeding. It is important that the cofeeding of metal precursor and Ti precursor produced a catalyst with a lower activity due to the coverage of the active metals by the Ti-O species [104]. Recently, Jiang et al. successfully prepared AuPt alloy cocatalyst-loaded TiO_2 by mixing chloroplatinic acid hexahydrate and chloroauric acid as the Pt and Au precursors, respectively [105]. The formation mechanism of AuPd-loaded TiO_2 particles and its nanostructures are presented in Figure 7a,e. The synergetic effects between Au and Pt reduced the agglomeration of metal particles, and CO poisoning was reduced. As a result, $AuPt/TiO_2$ could enhance catalytic CO oxidation by 20% at a low-temperature reaction of 100 °C in comparison to single-metal loading.

4.2. TiO_2/Non-Noble Metals/Oxides

Due to the high cost of noble metals, non-noble metals, such as Cu, Co and Ni, were alternatively used as cocatalysts to enhance the activities of TiO_2 [77,106,107,132–134]. In FS, these non-noble metals were loaded onto the TiO_2 via a single feed or a separated feed. Chen et al. used coflow FS to produce CuO/TiO_2 photocatalysts by mixing metal precursors composed of $Cu(NO_3)_2 \bullet 3H_2O$, ethanol and TBT. This mixture was injected into the burner of a CH_4/O_2 flame by a syringe pump [77]. Contrary to noble metals, such as Pt or Au, the addition of a Cu precursor led to changes in the crystal phases of TiO_2. The surface area of TiO_2 powder was reduced with the increase in the copper contents; interestingly, the specific surface area (SSA) was reduced from 98.96 to 70.07 $m^2 \cdot g^{-1}$ when the amount of Cu precursor was increased from 2% to 20%. However, the XRD data revealed that crystal size increased as the Cu content became higher. The rutile phase increased from 27.6% to 56.2% with the increase in the Cu content from 2% to 20%, respectively. Due to the fact of its small radius and lower valent state than Ti^{4+}, Cu^{2+} preferentially doped into TiO_2 lattices and created oxygen vacancies by reducing the Cu^{2+}. Since defective TiO_x species act as an important nucleation center, the percentage of the rutile phase increased as the Cu^{2+} doping content increased. However, at high concentrations, Cu could no longer dope into TiO_2. The excessive Cu^{2+} aggregated on the surface of the TiO_2 and formed CuO nanoparticles on the surface of the TiO_2. In the study, 20 wt.% CuO loading was the optimum composition for the combustion of lean CO, with a 95% conversion efficiency at 120 °C reaction [77]. Xiong et al. studied the synthesis of Cu/TiO_2 using FS and their CO_2

photoreaction under UV light [106]. They found that at a low Cu concentration, Cu^+ was rich and well dispersed into TiO_2 crystals. The maximum CO and CH_4 yields were 43.5 and 16.7 μmol g^{-1}, respectively, after a 4 h reaction. It was believed that the Cu^+ ions doped into the TiO_2 enhanced the charge separation and CO_2 absorption. Therefore, the Cu^+ ions incorporated into TiO_2 lattices facilitated the CO_2 activation, which was considered as an active site for CO_2 photoreduction [106].

Another work by Zhao et al. studied codoping on Pt-loaded TiO_2 by FS using cofeeding methods under a H_2/O_2 flame [107]. A small amount (1 wt.%) of $Co(NO_3)_2 \bullet 6H_2O$ added resulted in elemental doping into TiO_2 crystal. Therefore, mixing Co, Pt and Ti precursors produced Pt-nanoparticle-loaded codoped TiO_2 heterostructures. The codoping did not affect the particle sizes of TiO_2 supports, but reduced the Pt-particle's sizes from 2.47 nm to 0.72 nm with 1 wt.% codoping. With a high-temperature flame, Co^{2+} was oxidized to Co^{3+} and doped into the surface of the TiO_2. Doping with metals with different valence states induced more oxygen vacancies and suppressed the aggregation of Pt sub-nanoclusters. The catalytic activities of Pt/codoped TiO_2 for CO oxidation were much improved due to the rich oxygen absorbed on the surface of the defected codoped TiO_2. One hundred percent CO conversion was achieved by the Pt/codoped TiO_2 at a temperature of 70 °C, while it was achieved at 120 °C by Pt/TiO_2 [107].

4.3. TiO_2/Others

In addition to the above materials, FS was used for the synthesis of other composite structures with TiO_2, such as SnO_2/TiO_2 [135], Ga_2O_3/TiO_2 [136], MgO/TiO_2 [137], SiO_2/TiO_2 [138,139], $Ni-CeO_x-TiO_2$ [140], $WO_3/CeO_x/TiO_2$ [78,141], $Cr-Si-TiO_x$ [87], PbS/TiO_2 [142] and carbon/TiO_2 [96,143].

5. Summary and Outlooks

Flame synthesis has been considered as a potential method for the synthesis of nanoparticles, ranging from the lab scale to the industrial scale. Nanopowders prepared from flame synthesis usually exhibit unprecedented physicochemical properties in comparison to conventional synthetic methods. In addition, the flame synthesis can be continuous and fast, and changes in the various parameters may result in different product properties, which affect the catalytic performance. The direct conversion of TiO_2 particles from titanium precursors without any separation process or post-thermal annealing allows this method to produce TiO_2 products at a low cost in comparison to wet chemical methods. The properties of TiO_2 nanoparticles were controllable based on simple operational parameters, such as precursors and feeding types, precursor concentrations and compositions, gas flow rates and gas compositions, reaction atmospheres, and reaction temperatures. So far, TiO_2 nanoparticles with various morphologies, including spherical and particulate forms, were synthesized, and their crystal phases of TiO_2 (e.g., anatase and rutile) could be easily tuned. Advanced structures have become current trends in flame synthesis to improve the properties of TiO_2 nanoparticles according to the target applications. Typically, to deliver TiO_2 nanoparticles as a promising candidate for a sustainable world, TiO_2 must effectively work under solar light, which is an abundant and clean energy on Earth. Defect and bandgap engineering, such as doping and heterostructures, are demonstrated as powerful ways to improve the activities of TiO_2. Primary works have already reported the use of flame synthesis for defective and heterostructured TiO_2 nanoparticles. However, scaling up the reaction is vital in order to demonstrate the feasibility for industrial-scale synthesis.

There is still room for the development of high-quality defective and heterostructured TiO_2 nanoparticles:

(1) For achieving the industrial-scale production of flame-synthesized powder with well-defined characteristics, a deep understanding of the evaporation characteristics of the precursor solution, particle nucleation and growth, fluid–particle dynamics, etc., during flame synthesis is required for the design of reactors.

(2) Since flame synthesis involves the instantaneous evolution of powder, the degree of defects and the amount of dopants introduced in each TiO_2 nanoparticle can vary slightly. Therefore, more research on homogenizing the particles when prepared at a larger scale should be conducted.

(3) In terms of energy and environment, methods should be developed to clean or recycle gas that arises during the synthesis steps. In addition, efficient flame reactors should be designed in order to achieve low-energy consumption.

(4) The diversification of precursors for obtaining heterostructured TiO_2 nanoparticles is necessary. There could still be more elements that can be introduced for the synthesis of heterostructured TiO_2 particles.

References

1. Irshad, M.A.; Nawaz, R.; Rehman, M.Z.; Adrees, M.; Rizwan, M.; Ali, S.; Ahmad, S.; Tasleem, S. Synthesis, characterization and advanced sustainable applications of titanium dioxide nanoparticles: A review. *Ecotoxicol. Environ. Saf.* **2021**, *212*, 111978. [CrossRef] [PubMed]

2. Viana, M.M.; Soares, V.F.; Mohallem, N. Synthesis and characterization of TiO_2 nanoparticles. *Ceram. Int.* **2010**, *36*, 2047–2053. [CrossRef]

3. Nature. Tiny Tactics Transform Titanium Dioxide. *Nature Potfolio*; Springer: Cham, Switzerland, 2022. Available online: https://www.nature.com/articles/d42473-022-00068-3 (accessed on 30 December 2022).

4. Grand View Research Inc. *Titanium Dioxide Market Size, Share & Trends Analysis Report by Grade (Anatase, Rutile), by Production Process (Sulfate, Chloride), by Application (Paints & Coatings, Plastics), by Region, and Segment Forecasts, 2021–2028*; Grand View Resesarch Inc.: San Francisco, CA, USA, 2021. Available online: https://www.grandviewresearch.com/industry-analysis/titanium-dioxide-industry (accessed on 30 December 2022).

5. Fact.MR. *Titanium Dioxide Industry is Projected to Achieve a Global Market Size of US$ 25 bn by 2027, Currently East Asia Accounts for the Largest Share of over 30%.* 2022. Available online: https://www.globenewswire.com/en/news-release/2022/03/17/2404873/0/en/Titanium-Dioxide-Industry-is-Projected-to-Achieve-a-Global-Market-Size-of-US-25-Bn-by-2027-Currently-East-Asia-Accounts-for-the-Largest-Share-of-Over-30.html (accessed on 30 December 2022).

6. Promnopas, W.; Promnopas, S.; Phonkhokkong, T.; Thongtem, T.; Boonyawan, D.; Yu, L.; Wiranwetchayan, O.; Phuruangrat, A.; Thongtem, S. Crystalline phases and optical properties of titanium dioxide films deposited on glass substrates by microwave method. *Surf. Coat. Technol.* **2016**, *306*, 69–74. [CrossRef]

7. Zhao, W.; Li, Y.; Shen, W. Tuning the shape and crystal phase of TiO_2 nanoparticles for catalysis. *Chem. Commun.* **2021**, *57*, 6838–6850. [CrossRef] [PubMed]

8. Dette, C.; Pérez-Osorio, M.; Kley, C.; Punke, P.; Patrick, C.; Jacobson, P.; Giustino, F.; Jung, S.J.; Kern, K. TiO_2 anatase with a bandgap in the visible region. *Nano Lett.* **2014**, *14*, 6533–6538. [CrossRef]

9. Jiang, Z.; Xu, X.; Ma, Y.; Cho, S.H.; Ding, D.; Wang, C.; Wu, J.; Oleynikov, P.; Jia, M.; Cheng, J.; et al. Filling metal–organic framework mesopores with TiO_2 for CO_2 photoreduction. *Nature* **2020**, *586*, 549–554. [CrossRef]

10. Chong, R.; Li, J.; Ma, Y.; Zhang, B.; Han, H.; Li, C. Selective conversion of aqueous glucose to value-added sugar aldose on TiO_2-based photocatalysts. *J. Catal.* **2014**, *314*, 101–108. [CrossRef]

11. Inoue, T.; Fujishima, A.; Konishi, S.; Honda, K. Photoelectrocatalytic reduction of carbon dioxide in aqueous suspensions of semiconductor powders. *Nature* **1979**, *277*, 637–638. [CrossRef]

12. Hunge, Y.; Yadav, A.; Khan, S.; Takagi, K.; Suzuki, N.; Teshima, K.; Terashima, C.; Fujishima, A. Photocatalytic degradation of bisphenol A using titanium dioxide@nanodiamond composites under UV light illumination. *J. Colloid. Interface Sci.* **2021**, *582*, 1058–1066. [CrossRef]

13. Khan, S.; Kim, J.; Sotto, A.; Bruggen, B. Humic acid fouling in a submerged photocatalytic membrane reactor with binary TiO_2–ZrO_2 particles. *J. Ind. Eng. Chem.* **2015**, *21*, 779–786. [CrossRef]

14. Sunada, K.; Kikuchi, Y.; Hashimoto, K.; Fujishima, A. Bactericidal and detoxification effects of TiO_2 thin film photocatalysts. *Environ. Sci.Technol.* **1998**, *32*, 726–728. [CrossRef]

15. Fujishima, A.; Honda, K. Electrochemical photolysis of water at a semiconductor electrode. *Nature* **1972**, *238*, 37–38. [CrossRef]

16. Chen, X.; Liu, L.; Yu, P.; Mao, S. Increasing solar absorption for photocatalysis with black hydrogenated titanium dioxide nanocrystals. *Science* **2011**, *331*, 746–750. [CrossRef]

17. Naldoni, A.; Allieta, M.; Santangelo, S.; Marelli, M.; Fabbri, F.; Cappelli, S.; Bianchi, C.; Psaro, R.; Dal Santo, V. Effect of nature and location of defects on bandgap narrowing in black TiO_2 nanoparticles. *J. Am. Chem. Soc.* **2012**, *134*, 7600–7603. [CrossRef]

18. Choi, H.; Moon, S.-I.; Song, T.; Kim, S. Hydrogen-free defects in hydrogenated black TiO_2. *Phys. Chem. Chem. Phys.* **2018**, *20*, 19871–19876. [CrossRef]

19. Khan, S.; Je, M.; Kim, D.; Lee, S.; Cho, S.-H.; Song, T.; Choi, H. Mapping point defects of brookite TiO_2 for photocatalytic activity beyond anatase and P25. *J. Phys. Chem. C* **2020**, *124*, 10376–10384. [CrossRef]

20. Basavarajappa, P.S.; Patil, S.B.; Ganganagappa, N.; Reddy, K.R.; Raghu, A.V.; Reddy, C.V. Recent progress in metal-doped TiO_2, non-metal doped/codoped TiO_2 and TiO_2 nanostructured hybrids for enhanced photocatalysis. *Int. J. Hydrogen Energy* **2020**, *45*, 7764–7778. [CrossRef]

21. Liu, G.; Wang, L.; Yang, H.G.; Cheng, H.-M.; Lu, G.Q. Titania-based photocatalysts—Crystal growth, doping and heterostructuring. *J. Mater. Chem.* **2010**, *20*, 831–843. [CrossRef]

22. Khan, S.; Choi, H.; Kim, D.; Lee, S.Y.; Zhu, Q.; Zhang, J.; Kim, S.; Cho, S.-H. Self-assembled heterojunction of metal sulfides for improved photocatalysis. *Chem. Eng. J.* **2020**, *395*, 125092. [CrossRef]

23. Wang, H.; Zhang, L.; Chen, Z.; Hu, J.; Li, S.; Wang, Z.; Liu, J.; Wang, X. Semiconductor heterojunction photocatalysts: Design, construction, and photocatalytic performances. *Chem. Soc. Rev.* **2014**, *43*, 5234–5244. [CrossRef]

24. Low, J.; Yu, J.; Jaroniec, M.; Wageh, S.; Al-Ghamdi, A.A. Heterojunction photocatalysts. *Adv. Mater.* **2017**, *29*, 1601694. [CrossRef] [PubMed]

25. Choi, H.; Khan, S.; Choi, J.; Dinh, D.T.; Lee, S.Y.; Paik, U.; Cho, S.-H.; Kim, S. Synergetic control of band gap and structural transformation for optimizing TiO_2 photocatalysts. *Appl. Catal. B-Environ.* **2017**, *210*, 513–521. [CrossRef]

26. Scanlon, D.O.; Dunnill, C.W.; Buckeridge, J.; Shevlin, S.A.; Logsdail, A.J.; Woodley, S.M.; Catlow, C.R.A.; Powell, M.J.; Palgrave, R.G.; Parkin, I.P. Band alignment of rutile and anatase TiO_2. *Nature Mater.* **2013**, *12*, 798–801. [CrossRef] [PubMed]

27. Kawahara, T.; Konishi, Y.; Tada, H.; Tohge, N.; Nishii, J.; Ito, S. A patterned TiO_2 (anatase)/TiO_2(rutile) bilayer-type photocatalyst: Effect of the anatase/rutile junction on the photocatalytic activity. *Angew. Chem. Int. Ed.* **2002**, *114*, 2935–2937. [CrossRef]

28. Yang, D.; Liu, H.; Zheng, Z.; Yuan, Y.; Zhao, J.-C.; Waclawik, E.R.; Ke, X.; Zhu, H. An efficient photocatalyst structure: TiO_2(B) nanofibers with a shell of anatase nanocrystals. *J. Am. Chem. Soc.* **2009**, *131*, 17885–17893. [CrossRef]

29. An, X.; Hu, C.; Liu, H.; Qu, J. Hierarchical nanotubular anatase/rutile/TiO_2(B) heterophase junction with oxygen vacancies for enhanced photocatalytic H_2 production. *Langmuir* **2018**, *34*, 1883–1889. [CrossRef]

30. Jimmy, C.Y.; Yu, J.; Ho, W.; Zhang, L. Preparation of highly photocatalytic active nano-sized TiO_2 particles via ultrasonic irradiation. *Chem. Commun.* **2001**, 1942–1943. [CrossRef]

31. Marschall, R. Heterojunctions in composite photocatalysts. In *Solar Energy for Fuels*; Springer: Cham, Switzerland, 2015; pp. 143–172. [CrossRef]

32. Romero-Morán, A.; Sánchez-Salas, J.L.; Molina-Reyes, J. Influence of selected reactive oxygen species on the photocatalytic activity of TiO_2/SiO_2 composite coatings processed at low temperature. *Appl. Catal. B-Environ.* **2021**, *291*, 119685. [CrossRef]

33. Rani, S.; Garg, A.; Singh, N. Photocatalytic degradation and mineralization of amoxicillin and ofloxacin using TiO_2-SiO_2 composites. *Toxicol. Environ. Chem.* **2021**, *103*, 137–153. [CrossRef]

34. Robles-Melgarejo, M.; Espino-Valencia, J.; Natividad-Rangel, R.; Guevara-Martínez, S.J.; Rico-Cerda, J.L.; Rangel-Segura, R. Monoliths of TiO_2-SiO_2: Synthesis, characterization and photocatalytic activity. *J. Porous Mater.* **2021**, *28*, 1697–1711. [CrossRef]

35. Han, S.; Yu, L.; Zhang, H.; Chu, Z.; Chen, X.; Xi, H.; Long, J. Gold plasmon-enhanced solar hydrogen production over $SrTiO_3$/TiO_2 heterostructures. *Chem. Cat. Chem.* **2019**, *11*, 6203–6207. [CrossRef]

36. Wysmulek, K.; Sar, J.; Osewski, P.; Orlinski, K.; Kolodziejak, K.; Trenczek-Zajac, A.; Radecka, M.; Pawlak, D.A. A $SrTiO_3$-TiO_2 eutectic composite as a stable photoanode material for photoelectrochemical hydrogen production. *Appl. Catal. B-Environ.* **2017**, *206*, 538–546. [CrossRef]

37. Boro, B.; Gogoi, B.; Rajbongshi, B.; Ramchiary, A. Nano-structured TiO_2/ZnO nanocomposite for dye-sensitized solar cells application: A review. *Renew. Sustain. Energy Rev.* **2018**, *81*, 2264–2270. [CrossRef]

38. Rudakova, A.V.; Emeline, A.V.; Bahnemann, D.W. Effect of the TiO_2–ZnO heterostructure on the photoinduced hydrophilic conversion of TiO_2 and ZnO Surfaces. *J. Phys. Chem. C* **2019**, *123*, 8884–8891. [CrossRef]

39. Lin, L.; Yang, Y.; Men, L.; Wang, X.; He, D.; Chai, Y.; Zhao, B.; Ghoshroy, S.; Tang, Q. A highly efficient TiO_2@ZnO n–p–n heterojunction nanorod photocatalyst. *Nanoscale* **2013**, *5*, 588–593. [CrossRef]

40. Yaacob, N.; Sean, G.P.; Nazri, N.A.M.; Ismail, A.F.; Abidin, M.N.Z.; Subramaniam, M.N. Simultaneous oily wastewater adsorption and photodegradation by ZrO_2–TiO_2 heterojunction photocatalysts. *J. Water Process Eng.* **2021**, *39*, 101644. [CrossRef]

41. Fang, C.; Jiang, X.; Hu, J.; Song, J.; Sun, N.; Zhang, D.; Kuai, L. Ru nanoworms loaded TiO_2 for their catalytic performances toward CO oxidation. *ACS Appl. Mater. Interfaces* **2021**, *13*, 5079–5087. [CrossRef]

42. Moon, Y.K.; Jeong, S.Y.; Jo, Y.M.; Jo, Y.K.; Kang, Y.C.; Lee, J.H. Highly selective detection of benzene and discrimination of volatile aromatic compounds using oxide chemiresistors with tunable Rh-TiO$_2$ catalytic overlayers. *Adv. Sci.* **2021**, *8*, 2004078. [CrossRef]

43. Rozman, N.; Nadrah, P.; Cornut, R.; Jousselme, B.; Bele, M.; Dražić, G.; Gaberšček, M.; Kunej, Š.; Škapin, A.S. TiO$_2$ photocatalyst with single and dual noble metal co-catalysts for efficient water splitting and organic compound removal. *Int. J. Hydrogen Energy* **2021**, *46*, 32871–32881. [CrossRef]

44. Xia, C.; Nguyen, T.H.C.; Nguyen, X.C.; Kim, S.Y.; Nguyen, D.L.T.; Raizada, P.; Singh, P.; Nguyen, V.-H.; Nguyen, C.C.; Van Le, Q. Emerging cocatalysts in TiO$_2$-based photocatalysts for light-driven catalytic hydrogen evolution: Progress and perspectives. *Fuel* **2022**, *307*, 121745. [CrossRef]

45. Khan, S.; Kubota, Y.; Lei, W.; Suzuki, N.; Nakata, K.; Terashima, C.; Matsushita, N.; Fujishima, A.; Katsumata, K.-I. One-pot synthesis of (anatase/bronze-type)-TiO$_2$/carbon dot polymorphic structures and their photocatalytic activity for H$_2$ generation. *Appl. Surf. Sci.* **2020**, *526*, 146650. [CrossRef]

46. Meng, A.; Zhang, L.; Cheng, B.; Yu, J. Dual Cocatalysts in TiO$_2$ Photocatalysis. *Adv. Mater.* **2019**, *31*, 1807660. [CrossRef]

47. Ran, J.; Zhang, J.; Yu, J.; Jaroniec, M.; Qiao, S.Z. Earth-abundant cocatalysts for semiconductor-based photocatalytic water splitting. *Chem. Soc. Rev.* **2014**, *43*, 7787–7812. [CrossRef] [PubMed]

48. Wang, H.; You, T.; Shi, W.; Li, J.; Guo, L. Au/TiO$_2$/Au as a plasmonic coupling photocatalyst. *J. Phys. Chem. C* **2012**, *116*, 6490–6494. [CrossRef]

49. Awazu, K.; Fujimaki, M.; Rockstuhl, C.; Tominaga, J.; Murakami, H.; Ohki, Y.; Yoshida, N.; Watanabe, T. A plasmonic photocatalyst consisting of silver nanoparticles embedded in titanium dioxide. *J. Am. Chem. Soc.* **2008**, *130*, 1676–1680. [CrossRef]

50. Kumar, A.; Choudhary, P.; Kumar, A.; Camargo, P.H.; Krishnan, V. Recent advances in plasmonic photocatalysis based on TiO$_2$ and noble metal nanoparticles for energy conversion, environmental remediation, and organic synthesis. *Small* **2021**, *18*, 2101638. [CrossRef]

51. Khan, S.; Park, B.-I.; Han, J.S.; Lee, S.Y.; Cho, S.-H. Flame synthesized Y$_2$O$_3$:Tb^{3+}–Yb^{3+} phosphors as spectral convertors for solar cells. *Res. Chem. Intermed.* **2018**, *44*, 4619–4632. [CrossRef]

52. Khan, S.; Han, J.S.; Lee, S.Y.; Cho, S.-H. Flame-synthesized Y$_2$O$_3$:Tb^{3+} nanocrystals as spectral converting materials. *Nanopart. Res.* **2018**, *20*, 241. [CrossRef]

53. Khan, S.; Katsumata, K.-I.; Rodríguez-González, V.; Terashima, C.; Fujishima, A. Gas-phase synthesis for mass production of TiO$_2$ nanoparticles for environmental applications. In *Handbook of Nanomaterials and Nanocomposites for Energy and Environmental Applications*; Springer: Berlin/Heidelberg, Germany, 2020; pp. 1–21. [CrossRef]

54. Khan, S.; Choi, Y.; Ahn, H.-Y.; Han, J.H.; Ju, B.-K.; Chung, J.; Cho, S.-H. Control of Particle Size in Flame Spray Pyrolysis of Tb–doped Y$_2$O$_3$ for Bio-Imaging. *Materials* **2020**, *13*, 2987. [CrossRef]

55. Cho, S.-H.; Choi, Y.; Lee, S.; Byun; Young, J.; Khan, S. Fabricating Method of Titania Nanoparticles. Korean patent KR102044380B1, 13 November 2019. Available online: https://patents.google.com/patent/KR102044380B1/en?oq=KR102044380B1 (accessed on 30 December 2022).

56. Park, J.-S.; Kang, Y.C. Multicomponent (Mo, Ni) metal sulfide and selenide microspheres with empty nanovoids as anode materials for Na-ion batteries. *J. Mater. Chem. A* **2017**, *5*, 8616–8623. [CrossRef]

57. Park, J.-S.; Kang, Y.C. Uniquely structured Sb nanoparticle-embedded carbon/reduced graphene oxide composite shell with empty voids for high performance sodium-ion storage. *Chem. Eng. J.* **2019**, *373*, 227–237. [CrossRef]

58. Park, J.-S.; Yang, S.; Kang, Y.C. Prussian blue analogue nanocubes with hollow interior and porous walls encapsulated within reduced graphene oxide nanosheets and their sodium-ion storage performances. *Chem. Eng. J.* **2020**, *393*, 124606. [CrossRef]

59. Park, J.-S.; Kim, J.K.; Hong, J.H.; Cho, J.S.; Park, S.-K.; Kang, Y.C. Advances in the synthesis and design of nanostructured materials by aerosol spray processes for efficient energy storage. *Nanoscale* **2019**, *11*, 19012–19057. [CrossRef]

60. Park, J.-S.; Cho, J.S.; Kim, J.H.; Choi, Y.J.; Kang, Y.C. Electrochemical properties of micron-sized Co$_3$O$_4$ hollow powders consisting of size controlled hollow nanospheres. *J. Alloys Compd.* **2016**, *689*, 554–563. [CrossRef]

61. Sheng, Y.; Kraft, M.; Xu, R. Emerging applications of nanocatalysts synthesized by flame aerosol processes. *Curr. Opin. Chem. Eng.* **2018**, *20*, 39–49. [CrossRef]

62. Koirala, R.; Pratsinis, S.E.; Baiker, A. Synthesis of catalytic materials in flames: Opportunities and challenges. *Chem. Soc. Rev.* **2016**, *45*, 3053–3068. [CrossRef]

63. Li, S.; Ren, Y.; Biswas, P.; Stephen, D.T. Flame aerosol synthesis of nanostructured materials and functional devices: Processing, modeling, and diagnostics. *Prog. Energy Combust. Sci.* **2016**, *55*, 1–59. [CrossRef]

64. Teoh, W.Y. A perspective on the flame spray synthesis of photocatalyst nanoparticles. *Materials* **2013**, *6*, 3194–3212. [CrossRef]

65. Solakidou, M.; Georgiou, Y.; Deligiannakis, Y. Double-nozzle flame spray pyrolysis as a potent technology to engineer noble metal-TiO$_2$ nanophotocatalysts for efficient H$_2$ production. *Energies* **2021**, *14*, 817. [CrossRef]

66. Huo, J.; Hu, Y.; Jiang, H.; Huang, W.; Li, Y.; Shao, W.; Li, C. Mixed solvents assisted flame spray pyrolysis synthesis of TiO$_2$ hierarchically porous hollow spheres for dye-sensitized solar cells. *Ind. Eng. Chem. Res.* **2013**, *52*, 11029–11035. [CrossRef]

67. Mikaeili, F.; Topcu, S.; Jodhani, G.; Gouma, P.-I. Flame-sprayed pure and Ce-doped TiO$_2$ photocatalysts. *Catalysts* **2018**, *8*, 342. [CrossRef]

68. Memarzadeh, S.; Tolmachoff, E.D.; Phares, D.J.; Wang, H. Properties of nanocrystalline TiO$_2$ synthesized in premixed flames stabilized on a rotating surface. *Proc. Combust. Inst.* **2011**, *33*, 1917–1924. [CrossRef]

69. De Falco, G.; Ciardiello, R.; Commodo, M.; Del Gaudio, P.; Minutolo, P.; Porta, A.; D'Anna, A. TiO$_2$ nanoparticle coatings with advanced antibacterial and hydrophilic properties prepared by flame aerosol synthesis and thermophoretic deposition. *Surf. Coat. Technol.* **2018**, *349*, 830–837. [CrossRef]

70. Liu, C.; Camacho, J.; Wang, H. Phase equilibrium of TiO$_2$ nanocrystals in flame-assisted chemical vapor deposition. *Chem. Phys. Chem.* **2018**, *19*, 180–186. [CrossRef] [PubMed]

71. Yoon, J.D.; Park, K.Y.; Jang, H.D. Comparison of titania particles between oxidation of titanium tetrachloride and thermal decomposition of titanium tetraisopropoxide. *Aerosol Sci. Technol.* **2003**, *37*, 621–627. [CrossRef]

72. Yang, F.; Liu, M.; Chen, X.; Xu, Z.; Zhao, H. Simultaneous control over lattice doping and nanocluster modification of a hybrid CuO$_x$/TiO$_2$ photocatalyst during flame synthesis for enhancing hydrogen evolution. *Solar RRL* **2018**, *2*, 1870234. [CrossRef]

73. Park, H.K.; Park, K.Y. Control of particle morphology and size in vapor-phase synthesis of titania, silica and alumina nanoparticles. *KONA Powder Part. J.* **2015**, *32*, 85–101. [CrossRef]

74. Wu, S.; Wang, W.; Tu, W.; Yin, S.; Sheng, Y.; Manuputty, M.Y.; Kraft, M.; Xu, R. Premixed stagnation flame synthesized TiO$_2$ nanoparticles with mixed phases for efficient photocatalytic hydrogen generation. *ACS Sustain. Chem. Eng.* **2018**, *6*, 14470–14479. [CrossRef]

75. Manuputty, M.Y.; Dreyer, J.A.H.; Sheng, Y.; Bringley, E.J.; Botero, M.L.; Akroyd, J.; Kraft, M. Polymorphism of nanocrystalline TiO$_2$ prepared in a stagnation flame: Formation of the TiO$_{2-II}$ phase. *Chem. Sci.* **2019**, *10*, 1342–1350. [CrossRef]

76. Bi, W.; Hu, Y.; Jiang, H.; Yu, H.; Li, W.; Li, C. In-situ synthesized surface N-doped Pt/TiO$_2$ via flame spray pyrolysis with enhanced thermal stability for CO catalytic oxidation. *Appl. Surf. Sci.* **2019**, *481*, 360–368. [CrossRef]

77. Chen, X.; Xu, Z.; Yang, F.; Zhao, H. Flame spray pyrolysis synthesized CuO-TiO$_2$ nanoparticles for catalytic combustion of lean CO. *Proc. Combust. Instit.* **2019**, *37*, 5499–5506. [CrossRef]

78. Akurati, K.K.; Vital, A.; Dellemann, J.-P.; Michalow, K.; Graule, T.; Ferri, D.; Baiker, A. Flame-made WO$_3$/TiO$_2$ nanoparticles: Relation between surface acidity, structure and photocatalytic activity. *Appl. Catal. B-Environ.* **2008**, *79*, 53–62. [CrossRef]

79. Smirniotis, P.G.; Boningari, T.; Inturi, S.N.R. Single-step synthesis of N-doped TiO$_2$ by flame aerosol method and the effect of synthesis parameters. *Aerosol Sci. Technol.* **2018**, *52*, 913–922. [CrossRef]

80. Smirniotis, P.G.; Boningari, T.; Damma, D.; Inturi, S.N.R. Single-step rapid aerosol synthesis of N-doped TiO$_2$ for enhanced visible light photocatalytic activity. *Catal. Commun.* **2018**, *113*, 1–5. [CrossRef]

81. Shahid, M.; Farooqi, Z.H.; Begum, R.; Arif, M.; Irfan, A.; Azam, M. Extraction of cobalt ions from aqueous solution by microgels for in-situ fabrication of cobalt nanoparticles to degrade toxic dyes: A two fold-environmental application. *Chem. Phys. Lett.* **2020**, *754*, 137645. [CrossRef]

82. Arif, M.; Farooqi, Z.H.; Irfan, A.; Begum, R. Gold nanoparticles and polymer microgels: Last five years of their happy and successful marriage. *J. Mol. Liq.* **2021**, *336*, 116270. [CrossRef]

83. Xu, C.; Ravi Anusuyadevi, P.; Aymonier, C.; Luque, R.; Marre, S. Nanostructured materials for photocatalysis. *Chem. Soc. Rev.* **2019**, *48*, 3868–3902. [CrossRef] [PubMed]

84. Huo, J.; Hu, Y.; Jiang, H.; Li, C. In situ surface hydrogenation synthesis of Ti^{3+} self-doped TiO$_2$ with enhanced visible light photoactivity. *Nanoscale* **2014**, *6*, 9078–9084. [CrossRef] [PubMed]

85. Lin, L.-Y.; Kavadiya, S.; He, X.; Wang, W.-N.; Karakocak, B.B.; Lin, Y.-C.; Berezin, M.Y.; Biswas, P. Engineering stable Pt nanoparticles and oxygen vacancies on defective TiO$_2$ via introducing strong electronic metal-support interaction for efficient CO$_2$ photoreduction. *Chem. Eng. J.* **2019**, *389*, 123450. [CrossRef]

86. Wu, S.; Manuputty, M.Y.; Sheng, Y.; Wang, H.; Yan, Y.; Kraft, M.; Xu, R. Flame synthesized blue TiO$_{2-x}$ with tunable oxygen vacancies from surface to grain boundary to bulk. *Small Methods* **2021**, *5*, 2000928. [CrossRef]

87. Inturi, S.N.R.; Boningari, T.; Suidan, M.; Smirniotis, P.G. Stabilization of Cr in Ti/Si/Cr ternary composites by aerosol flame spray-assisted synthesis for visible-light-driven photocatalysis. *Ind. Eng. Chem. Res.* **2016**, *55*, 11839–11849. [CrossRef]

88. Inturi, S.N.R.; Boningari, T.; Suidan, M.; Smirniotis, P.G. Visible-light-induced photodegradation of gas phase acetonitrile using aerosol-made transition metal (V, Cr, Fe, Co, Mn, Mo, Ni, Cu, Y, Ce, and Zr) doped TiO$_2$. *Appl. Catal. B-Environ.* **2014**, *144*, 333–342. [CrossRef]

89. Inturi, S.N.R.; Boningari, T.; Suidan, M.; Smirniotis, P.G. Flame aerosol synthesized Cr incorporated TiO$_2$ for visible light photodegradation of gas phase acetonitrile. *J. Phys. Chem. C* **2014**, *118*, 231–242. [CrossRef]

90. Wang, Z.-M.; Sahle-Demessie, E.; Aly Hassan, A. Selective oxidation using flame aerosol synthesized iron and vanadium-doped nano-TiO$_2$. *J. Nanotechnol.* **2011**, *2011*, 209150. [CrossRef]

91. Teleki, A.; Bjelobrk, N.; Pratsinis, S.E. Flame-made Nb-and Cu-doped TiO$_2$ sensors for CO and ethanol. *Sens. Actuators B Chem.* **2008**, *130*, 449–457. [CrossRef]

92. Teoh, W.Y.; Amal, R.; Mädler, L.; Pratsinis, S.E. Flame sprayed visible light-active Fe-TiO$_2$ for photomineralisation of oxalic acid. *Catal. Today* **2007**, *120*, 203–213. [CrossRef]

93. Hu, Y.; Jiang, H.; Li, Y.; Wang, B.; Zhang, L.; Li, C.; Wang, Y.; Cohen, T.; Jiang, Y.; Biswas, P. Engineering the outermost layers of TiO$_2$ nanoparticles using in situ Mg doping in a flame aerosol reactor. *AIChE J.* **2017**, *63*, 870–880. [CrossRef]

94. Dozzi, M.V.; Zuliani, A.; Grigioni, I.; Chiarello, G.L.; Meda, L.; Selli, E. Photocatalytic activity of one step flame-made fluorine doped TiO$_2$. *Appl. Catal. A-General* **2016**, *521*, 220–226. [CrossRef]

95. Boningari, T.; Inturi, S.N.R.; Suidan, M.; Smirniotis, P.G. Novel one-step synthesis of sulfur doped-TiO$_2$ by flame spray pyrolysis for visible light photocatalytic degradation of acetaldehyde. *Chem. Eng. J.* **2018**, *339*, 249–258. [CrossRef]

96. Pennington, A.M.; Halim, H.; Shi, J.; Kear, B.H.; Celik, F.E.; Tse, S.D. Low-pressure flame synthesis of carbon-stabilized TiO_{2-II} (srilankite) nanoparticles. *J. Aerosol Sci.* **2021**, *156*, 105775. [CrossRef]

97. Boningari, T.; Inturi, S.N.R.; Suidan, M.; Smirniotis, P.G. Novel one-step synthesis of nitrogen-doped TiO_2 by flame aerosol technique for visible-light photocatalysis: Effect of synthesis parameters and secondary nitrogen (N) source. *Chem. Eng. J.* **2018**, *350*, 324–334. [CrossRef]

98. Huo, J.; Hu, Y.; Jiang, H.; Hou, X.; Li, C. Continuous flame synthesis of near surface nitrogen doped TiO_2 for dye-sensitized solar cells. *Chem. Eng. J.* **2014**, *258*, 163–170. [CrossRef]

99. Gao, F.; Xu, Z.; Zhao, H. Flame spray pyrolysis made Pt/TiO_2 photocatalysts with ultralow platinum loading and high hydrogen production activity. *Proc. Combust. Instit.* **2021**, *38*, 6503–6511. [CrossRef]

100. Chiarello, G.L.; Dozzi, M.V.; Scavini, M.; Grunwaldt, J.-D.; Selli, E. One step flame-made fluorinated Pt/TiO_2 photocatalysts for hydrogen production. *Appl. Catal. B-Environ.* **2014**, *160–161*, 144–151. [CrossRef]

101. Fujiwara, K.; Müller, U.; Pratsinis, S.E. Pd subnano-clusters on TiO_2 for solar-light removal of NO. *ACS Catal.* **2016**, *6*, 1887–1893. [CrossRef]

102. Fujiwara, K.; Pratsinis, S.E. Single Pd atoms on TiO_2 dominate photocatalytic NO_x removal. *Appl. Catal. B-Environ.* **2018**, *226*, 127–134. [CrossRef]

103. Chiarello, G.L.; Selli, E.; Forni, L. Photocatalytic hydrogen production over flame spray pyrolysis-synthesised TiO_2 and Au/TiO_2. *Appl. Catal. B-Environ.* **2008**, *84*, 332–339. [CrossRef]

104. Pongthawornsakun, B.; Mekasuwandumrong, O.; Santos Aires, F.J.C.; Büchel, R.; Baiker, A.; Pratsinis, S.E.; Panpranot, J. Variability of particle configurations achievable by 2-nozzle flame syntheses of the $Au-Pd-TiO_2$ system and their catalytic behaviors in the selective hydrogenation of acetylene. *Appl. Catal. A-General* **2018**, *549*, 1–7. [CrossRef]

105. Jiang, J.; Lei, J.; Hu, Y.; Bi, W.; Xu, N.; Li, Y.; Chen, X.; Jiang, H.; Li, C. Electron transfer effect from Au to Pt in $Au-Pt/TiO_2$ towards efficient catalytic activity in CO oxidation at low temperature. *Appl. Surf. Sci.* **2020**, *521*, 146447. [CrossRef]

106. Xiong, Z.; Xu, Z.; Li, Y.; Dong, L.; Wang, J.; Zhao, J.; Chen, X.; Zhao, Y.; Zhao, H.; Zhang, J. Incorporating highly dispersed and stable Cu_+ into TiO_2 lattice for enhanced photocatalytic CO_2 reduction with water. *Appl. Surf. Sci.* **2020**, *507*, 145095. [CrossRef]

107. Zhao, X.; Hu, Y.; Jiang, H.; Yu, J.; Jiang, R.; Li, C. Engineering TiO_2 supported Pt sub-nanoclusters via introducing variable valence Co ion in high-temperature flame for CO oxidation. *Nanoscale* **2018**, *10*, 13384–13392. [CrossRef]

108. Davydov, L.; Reddy, E.P.; France, P.; Smirniotis, P.G. Transition-metal-substituted titania-loaded MCM-41 as photocatalysts for the degradation of aqueous organics in visible light. *J. Catal.* **2001**, *203*, 157–167. [CrossRef]

109. Reddy, E.P.; Sun, B.; Smirniotis, P.G. Transition metal modified TiO_2-loaded MCM-41 catalysts for visible- and UV-light driven photodegradation of aqueous organic pollutants. *J. Phys. Chem. B* **2004**, *108*, 17198–17205. [CrossRef]

110. Sun, B.; Reddy, E.P.; Smirniotis, P.G. Effect of the Cr^{6+} concentration in Cr-incorporated TiO_2-loaded MCM-41 catalysts for visible light photocatalysis. *Appl. Catal. B-Environ.* **2005**, *57*, 139–149. [CrossRef]

111. Herrmann, J.-M. Fundamentals and misconceptions in photocatalysis. *J. Photochem. Photobiol. A-Chem.* **2010**, *216*, 85–93. [CrossRef]

112. Sun, B.; Reddy, E.P.; Smirniotis, P.G. TiO_2-loaded Cr-modified molecular sieves for 4-chlorophenol photodegradation under visible light. *J. Catal.* **2006**, *237*, 314–321. [CrossRef]

113. Chaisuk, C.; Wehatoranawee, A.; Preampiyawat, S.; Netiphat, S.; Shotipruk, A.; Mekasuwandumrong, O. Preparation and characterization of CeO_2/TiO_2 nanoparticles by flame spray pyrolysis. *Ceram. Int.* **2011**, *37*, 1459–1463. [CrossRef]

114. Michalow-Mauke, K.A.; Lu, Y.; Kowalski, K.; Graule, T.; Nachtegaal, M.; Kröcher, O.; Ferri, D. Flame-made WO_3/CeO_x-TiO_2 catalysts for selective catalytic reduction of NO_x by NH_3. *ACS Catal.* **2015**, *5*, 5657–5672. [CrossRef]

115. Bahmanrokh, G.; Cazorla, C.; Mofarah, S.S.; Shahmiri, R.; Yao, Y.; Ismail, I.; Chen, W.-F.; Koshy, P.; Sorrell, C.C. Band gap engineering of Ce-doped anatase TiO_2 through solid solubility mechanisms and new defect equilibria formalism. *Nanoscale* **2020**, *12*, 4916–4934. [CrossRef]

116. Yoo, M.; Yu, Y.-S.; Ha, H.; Lee, S.; Choi, J.-S.; Oh, S.; Kang, E.; Choi, H.; An, H.; Lee, K.-S. A tailored oxide interface creates dense Pt single-atom catalysts with high catalytic activity. *Energy Environ. Sci.* **2020**, *13*, 1231–1239. [CrossRef]

117. Choi, H.; Shin, D.; Yeo, B.C.; Song, T.; Han, S.S.; Park, N.; Kim, S. Simultaneously controllable doping sites and the activity of a W–N codoped TiO_2 Photocatalyst. *ACS Catal.* **2016**, *6*, 2745–2753. [CrossRef]

118. Ansari, S.A.; Khan, M.M.; Ansari, M.O.; Cho, M.H. Nitrogen-doped titanium dioxide (N-doped TiO_2) for visible light photocatalysis. *New J. Chem.* **2016**, *40*, 3000–3009. [CrossRef]

119. Boningari, T.; Inturi, S.N.R.; Suidan, M.; Smirniotis, P.G. Novel continuous single-step synthesis of nitrogen-modified TiO_2 by flame spray pyrolysis for photocatalytic degradation of phenol in visible light. *J. Mater. Sci. Technol.* **2018**, *34*, 1494–1502. [CrossRef]

120. Pisduangdaw, S.; Mekasuwandumrong, O.; Fujita, S.-I.; Arai, M.; Yoshida, H.; Panpranot, J. One step synthesis of $Pt–Co/TiO_2$ catalysts by flame spray pyrolysis for the hydrogenation of 3-nitrostyrene. *Catal. Commun.* **2015**, *61*, 11–15. [CrossRef]

121. Ernst, F.O.; Büchel, R.; Strobel, R.; Pratsinis, S.E. One-step flame-synthesis of carbon-embedded and-supported platinum clusters. *Chem. Mater.* **2008**, *20*, 2117–2123. [CrossRef]

122. Fujiwara, K.; Pratsinis, S.E. Atomically dispersed Pd on nanostructured TiO_2 for NO removal by solar light. *AIChE J.* **2017**, *63*, 139–146. [CrossRef]

123. Mekasuwandumrong, O.; Phothakwanpracha, S.; Jongsomjit, B.; Shotipruk, A.; Panpranot, J. Liquid-phase selective hydrogenation of 1-heptyne over Pd/TiO$_2$ catalyst synthesized by one-step flame spray pyrolysis. *Catal. Lett.* **2010**, *136*, 164–170. [CrossRef]

124. Zong, Y.; Li, S.; Niu, F.; Yao, Q. Direct synthesis of supported palladium catalysts for methane combustion by stagnation swirl flame. *Proc. Combust. Instit.* **2015**, *35*, 2249–2257. [CrossRef]

125. Mädler, L.; Stark, W.J.; Pratsinis, S.E. Simultaneous deposition of Au nanoparticles during flame synthesis of TiO$_2$ and SiO$_2$. *J. Mater. Res.* **2003**, *18*, 115–120. [CrossRef]

126. Pisduangdaw, S.; Mekasuwandumrong, O.; Yoshida, H.; Fujita, S.-I.; Arai, M.; Panpranot, J. Flame-made Pt/TiO$_2$ catalysts for the liquid-phase selective hydrogenation of 3-nitrostyrene. *Appl. Catal. A-General* **2015**, *490*, 193–200. [CrossRef]

127. Teoh, W.Y.; Mädler, L.; Amal, R. Inter-relationship between Pt oxidation states on TiO$_2$ and the photocatalytic mineralisation of organic matters. *J. Catal.* **2007**, *251*, 271–280. [CrossRef]

128. Chomkitichai, W.; Ninsonthi, H.; Liewhiran, C.; Wisitsoraat, A.; Sriwichai, S.; Phanichphant, S. Flame-made Pt-loaded TiO$_2$ thin films and their application as H$_2$ gas sensors. *J. Nanomater.* **2013**, *2013*, 497318. [CrossRef]

129. Teoh, W.Y.; Mädler, L.; Beydoun, D.; Pratsinis, S.E.; Amal, R. Direct (one-step) synthesis of TiO$_2$ and Pt/TiO$_2$ nanoparticles for photocatalytic mineralisation of sucrose. *Chem. Eng. Sci.* **2005**, *60*, 5852–5861. [CrossRef]

130. Johannessen, T.; Koutsopoulos, S. One-step flame synthesis of an active Pt/TiO$_2$ Catalyst for SO$_2$ oxidation—A possible alternative to traditional methods for parallel screening. *J. Catal.* **2002**, *205*, 404–408. [CrossRef]

131. Chomkitichai, W.; Tamaekong, N.; Liewhiran, C.; Wisitsoraat, A.; Sriwichai, S.; Phanichphant, S. H$_2$ sensor based on Au/TiO$_2$ nanoparticles by flame spray pyrolysis. *Eng. J.* **2012**, *16*, 135–142. [CrossRef]

132. Himabindu, V.; Srilatha, K.; Bhagawan, D.; Srinivasulu, D. Comparison study between Ni/TiO$_2$ and Ni/flame synthesized TiO$_2$ catalysts for hydrogen production using thermocatalytic decomposition of methane. *S. Afr. J. Chem. Eng.* **2018**, *25*, 91–97. Available online: https://hdl.handle.net/10520/EJC-1034aff3ba (accessed on 30 December 2022).

133. Tian, X.; Su, M.; Zhao, H. Kinetics of redox reactions of CuO@TiO$_2$–Al$_2$O$_3$ for chemical looping combustion and chemical looping with oxygen uncoupling. *Combust. Flame* **2020**, *213*, 255–267. [CrossRef]

134. Meng, L.; Zhao, H. Low-temperature complete removal of toluene over highly active nanoparticles CuO-TiO$_2$ synthesized via flame spray pyrolysis. *Appl. Catal. B-Environ* **2020**, *264*, 118427. [CrossRef]

135. Akurati, K.K.; Vital, A.; Hany, R.; Bommer, B.; Graule, T.; Winterer, M. One-step flame synthesis of SnO$_2$/TiO$_2$ composite nanoparticles for photocatalytic applications. *Int. J. Photoenergy* **2005**, *7*, 153–161. [CrossRef]

136. Koirala, R.; Buechel, R.; Krumeich, F.; Pratsinis, S.E.; Baiker, A. Oxidative dehydrogenation of ethane with CO$_2$ over flame-made Ga-loaded TiO$_2$. *ACS Catal.* **2015**, *5*, 690–702. [CrossRef]

137. Shrestha, K.M.; Sorensen, C.M.; Klabunde, K.J. MgO–TiO$_2$ mixed oxide nanoparticles: Comparison of flame synthesis versus aerogel method; characterization, and photocatalytic activities. *J. Mater. Res.* **2013**, *28*, 431–439. [CrossRef]

138. Liu, J.; He, G.; Lu, N.; Li, J. Fabrication of photo-absorption enhanced black TiO$_2$–SiO$_2$ by flame spraying. *Mater. Res. Express* **2017**, *4*, 125503. [CrossRef]

139. Fang, J.; Wang, Y.; Attoui, M.; Chadha, T.S.; Ray, J.R.; Wang, W.-N.; Jun, Y.-S.; Biswas, P. Measurement of sub-2 nm clusters of pristine and composite metal oxides during nanomaterial synthesis in flame aerosol reactors. *Anal. Chem.* **2014**, *86*, 7523–7529. [CrossRef] [PubMed]

140. Kho, E.T.; Lovell, E.; Wong, R.J.; Scott, J.; Amal, R. Manipulating ceria-titania binary oxide features and their impact as nickel catalyst supports for low temperature steam reforming of methane. *Appl. Catal. A-General* **2017**, *530*, 111–124. [CrossRef]

141. Ramadhan, Z.R.; Yun, C.; Park, B.-I.; Yu, S.; Kang, M.H.; Kim, S.; Lim, D.; Choi, B.H.; Han, J.W.; Kim, Y.H. High performance electrochromic devices based on WO$_3$TiO$_2$ nanoparticles synthesized by flame spray pyrolysis. *Opt. Mater.* **2019**, *89*, 559–562. [CrossRef]

142. Bubenhofer, S.B.; Schumacher, C.M.; Koehler, F.M.; Luechinger, N.A.; Grass, R.N.; Stark, W.J. Large-scale synthesis of PbS–TiO$_2$ heterojunction nanoparticles in a single step for solar cell application. *J. Phys. Chem. C* **2012**, *116*, 16264–16270. [CrossRef]

143. Hou, D.; Mao, Q.; Ren, Y.; Luo, K.H. Atomic insights into mechanisms of carbon coating on titania nanoparticle during flame synthesis. *Carbon* **2023**, *201*, 189–199. [CrossRef]